

The Evolution of Turbulence Producing Motions in the ABL Across a Natural Roughness Transition

Justin P. Cooke¹, Douglas J. Jerolmack^{1,2}, & George Ilhwan Park¹

¹Department of Mechanical Engineering and Applied Mechanics, University of Pennsylvania, Philadelphia, Pennsylvania, USA

²Department of Earth and Environmental Science, University of Pennsylvania, Philadelphia, Pennsylvania, USA

Key Points:

- When atmospheric flows encounter roughness transitions an Internal Boundary Layer forms and changes the structure of the flow within
- Internal boundary layers set the new length-scales of the flow and control turbulence producing motions
- The structure of turbulence producing events is shown to scale with Internal Boundary Layer height with implications for sediment transport

arXiv:2406.05163v1 [physics.flu-dyn] 7 Jun 2024

Corresponding author: George Ilhwan Park, gipark@seas.upenn.edu

Abstract

Landforms such as sand dunes act as roughness elements to Atmospheric Boundary Layer (ABL) flows, triggering the development of new scales of turbulent motions. These turbulent motions, in turn, energize and kick-up sand particles, influencing sediment transport and ultimately the formation and migration of dunes – with knock on consequences for dust emission. While feedbacks between flow and form have been studied at the scale of dunes, research has not examined how the development of an Internal Boundary Layer (IBL) over the entire dune field influences sediment-transporting turbulence. Here, we deploy large-eddy simulation of an ABL encountering a natural roughness transition: the sand dunes at White Sands National Park, New Mexico. We analyze turbulence producing motions and how they change as the IBL grows over the dune field. Frequency spectrum and Reynolds shear stress profiles show that IBL thickness determines the largest scales of turbulence. More, the developing IBL enhances the frequency, magnitude and duration of sweep and ejection events – turbulence producing motions whose peaks systematically migrate away from the wall as the IBL thickens. Because sweep and ejection events are known to drive sediment transport, our findings provide a mechanism for coupling the co-evolution of the landscape and the ABL flow over it. More broadly, our results have implications for how roughness transitions influence the transport of pollutants, particulates, heat, and moisture.

1 Introduction

The Atmospheric Boundary Layer (ABL) is the $O(10^2-10^3)$ m thick region near the Earth’s surface that most feels the shear stresses of the flow (Abedi et al., 2021; Bou-Zeid et al., 2020; Gul & Ganapathisubramani, 2022). Owing to the large length-scales and the heterogeneous topography of the Earth, ABL flows are highly turbulent, with the friction Reynolds numbers $Re_\tau \sim O(10^6-10^7)$. Complex terrain, composed of mountains, forests, hills, and valleys, as well as areas composed of human-made structures, such as urban areas and wind farms, act as roughness elements within the ABL, and present challenges to our understanding (Vanderwel & Ganapathisubramani, 2019; Bou-Zeid et al., 2020; W. Li & Giometto, 2023). In cities, public health is impacted by the interactions between the ABL and buildings, influencing fluxes of heat and pollutants (D. Li & Bou-Zeid, 2013; Manoli et al., 2019; W. Li & Giometto, 2023). The growing intensity of wildfires in North America has also shown the importance of the ABL in transporting smoke, with cascading consequences for public health (Zhou et al., 2023; Gould et al., 2024; Ceamanos et al., 2023). The presence of roughness induces changes to the transport of particles, heat, and momentum within the ABL – especially near the Earth’s surface – so understanding the physical mechanisms of these changes is critical for prediction and modeling capabilities.

Aeolian sand dunes, which can reach roughness heights (k) taller than 100m (Gunn et al., 2022), impede the flow of the ABL, and alter coherent flow structures (Wiggs & Weaver, 2012; Anderson & Chamecki, 2014; Wang & Anderson, 2019; Bristow et al., 2021). The spatial variation in flow over dune topography results in spatial patterns in sand transport across dunes (Bagnold, 1941), which are ultimately connected to the structure and intensity of turbulence forced by roughness (Bauer et al., 2013; Bristow et al., 2021; Tan et al., 2023). Entrainment of sand is often driven by turbulent ejection events and, once a threshold velocity is met, sand is transported primarily by sweeping motions (Sterk et al., 1998; Leenders et al., 2005; Wiggs & Weaver, 2012; Bauer et al., 2013; Rana et al., 2021). Sand entrainment, and the associated turbulent motions, are also responsible for dust emission (Kok et al., 2012; Parajuli et al., 2016; J. Zhang et al., 2022).

Sand dunes have been shown to increase the frequency and intensity of turbulent events that drive sand transport (Bristow et al., 2021; Tan et al., 2023). Due to the challenges and complications associated with collecting time- and height-based velocity data

over large areas in field campaigns (Abedi et al., 2021; Bell et al., 2020), and the stringent costs of simulating large-scale atmospheric flows (Bou-Zeid et al., 2020; Stoll et al., 2020), much of the prior work on flows over dunes has been restricted to isolated (Wiggs & Weaver, 2012; Bristow et al., 2021, 2022) or small clusters (Anderson & Chamecki, 2014; Wang & Anderson, 2019) of dunes. What happens, however, when flow over a smooth surface encounters a train of dunes? Step changes in surface roughness (smooth-to-rough, rough-to-smooth, rough-to-rougher, and vice versa) trigger the formation an Internal Boundary Layer (IBL) (Antonia & Luxton, 1972a, 1972b; Hanson & Ganapathisubramani, 2016; Gul & Ganapathisubramani, 2022). Within the IBL, the flow gradually adapts to the new near-surface condition, while outside, the flow largely retains the characteristics of the upstream boundary layer. Gul and Ganapathisubramani (2022) showed that the IBL acts as a ‘shield’, as the outer region of their rough-to-smooth flow loses spectral energy. Additionally, the IBL was shown to influence the scale-interaction between the large- and small-scale motions. Our previous work (Cooke et al., 2024) used an amplitude modulation analysis to quantify this interaction with the Amplitude Modulation Coefficient R_{AM} , and discovered a shifting of the negative correlation peak away from the wall with increasing distance from the transition. The negative peak has been attributed to intermittency between the outer portion of the boundary layer, and the freestream (Mathis et al., 2009). Due to the increased roughness, we expect that sand dunes will extract more momentum from the flow compared to a smooth surface; and therefore that the wind speed and associated turbulent stresses will progressively decline as the IBL thickens (Jerolmack et al., 2012; Gunn et al., 2020). How does this manifest, in terms of the spatial pattern of turbulence producing motions, over an entire dune field?

White Sands National Park (New Mexico, USA) presents a case study in how development of an IBL, triggered by a roughness transition, can lead to feedbacks between flow and form that affect the evolution of an entire dune field (Jerolmack et al., 2012). In this landscape a quasi-unidirectional wind encounters an abrupt roughness increase from smooth playa to sand dunes, whose size grows rapidly over the first several kilometers and then gradually declines over the next 10 km. The observed spatial pattern of sand flux is broadly similar; first increasing rapidly and then gradually declining moving downwind (Jerolmack et al., 2012; Gunn et al., 2020). Spatially sparse wind observations are consistent with a simplified analytical model, that describes a pattern of gradual downwind decrease in surface-wind velocity due to a developing IBL (Gunn et al., 2020). Our prior work used Large Eddy Simulations (LES) over White Sands topography in order to resolve the complex flows that give rise to IBL development across the dune field (Cooke et al., 2024). These simulations substantiated the importance of IBL development on sand-dune dynamics, while revealing a novel self-similar structure for the vertical Reynolds stress profile that is scaled by the height of the IBL. The current paper builds directly on this last result.

Here we use LES numerical data from our previous study (Cooke et al., 2024) to investigate the evolution of turbulence producing motions that arise in the developing IBL across the White Sands dune field. We first provide a brief overview of the theory behind the analysis. We then describe the wall-modeled LES deployed to simulate a neutrally buoyant ABL flow encountering a spatially heterogeneous roughness transition, including a domain sensitivity analysis. We find that both the magnitude and height (above the bed) of turbulence producing motions are set by the scale of the developing IBL, which creates a spatial pattern of turbulence across the dune field. We consider the implications of this pattern for sediment transport and dune dynamics at White Sands, and also more broadly for other landscapes.

2 Theory

2.1 Internal Boundary Layer Height Estimation

For flows encountering a roughness transition, there are simple correlations for predicting the evolution of the IBL height (δ_i) as a function of the upstream and downstream roughness parameters, z_{01} and z_{02} , respectively (Elliott, 1958; Townsend, 1965; Panofsky, 1973; Wood, 1982; Panofsky & Dutton, 1984; Pendergrass & Aria, 1984; Savelyev & Taylor, 2001). These correlations were recently tested in detail by Gul and Ganapathisubramani (2022), and the simplest reasonable model is of the form

$$\frac{\delta_i}{z_0} = a \left(\frac{\hat{x}}{z_0} \right)^b. \quad (1)$$

Here, a and b are empirical constants, and $\hat{x} = x - x_0$ is the streamwise distance from the location x_0 where the roughness transition occurs. The roughness parameter, z_0 , may be chosen to be the larger of the two, or simply the downstream value. Typically, $b = 0.8$, but a wide range of values ($b = 0.2-0.8$) have been reported in the literature (Gul & Ganapathisubramani, 2022). Measured data of developing IBL thickness δ_i are often fit to an equation of the form in Equation 1.

What defines the boundary of the IBL? Many methods to determine δ_i exist in the literature (Gul & Ganapathisubramani, 2022). Most are based on differences of wall-normal velocity gradients (Elliott, 1958), with others based on streamwise differences in flow variables such as turbulence intensity (M. Li et al., 2021). Following our previous study (Cooke et al., 2024) we choose the latter method, which uses the following equation:

$$\Delta \left[\frac{\langle u'u' \rangle(x, z)}{U_\infty^2} \right] / \Delta \left[\log_{10} \left(\frac{\hat{x}}{\delta} \right) \right] \rightarrow 0. \quad (2)$$

Equation 2 describes the difference of the normalized value of $\langle u'u' \rangle$, which is a function of streamwise (x) and wall-normal (z) coordinates, divided by the normalized distance between log-spaced streamwise stations. The value of δ_i at the upstream streamwise station is determined as the wall-normal height in which this difference approaches zero. Here, U_∞ is the freestream velocity. For our simulations we choose a threshold value of 10^{-4} to represent convergence toward zero in Equation 2. This method has been previously compared against others in Gul and Ganapathisubramani (2022), and was found to perform favorably.

2.2 Quadrant Analysis

A good indicator of turbulence production is the Reynolds shear stress, $\langle u'w' \rangle$, and one method to understand its generation is quadrant analysis (Wallace et al., 1972; Willmarth & Lu, 1972). Quadrant analysis has been used to analyze smooth wall-bounded flows (Wallace et al., 1972; Willmarth & Lu, 1972), rough wall-bounded flows (Raupach, 1981; Choi et al., 1993; Bristow et al., 2021), ABL flows (Lin et al., 1997; Q. Li & Bou-Zeid, 2019), and flows encountering a roughness transition (Gul & Ganapathisubramani, 2022). A comprehensive review of quadrant analysis and its use is provided in Wallace (2016). The basic premise is to decompose the product of streamwise and wall-normal velocity fluctuations, u' and w' , respectively, into four groups to understand the transfer of momentum. These groups are characterized as outward interactions (Q_1 ; $u' > 0$, $w' > 0$), ejections (Q_2 ; $u' < 0$, $w' > 0$), inward interactions (Q_3 ; $u' < 0$, $w' < 0$), and sweeps (Q_4 ; $u' > 0$, $w' < 0$) (Wallace et al., 1972; Wallace, 2016). Under the background mean shear with $\partial U / \partial y > 0$, Q_1 and Q_3 motions do not positively contribute, but rather decrease $\langle u'w' \rangle$; conversely, Q_2 and Q_4 motions augment $\langle u'w' \rangle$, acting as turbulence producing motions (Wallace et al., 1972; Willmarth & Lu, 1972). Contributions

of each quadrant to the overall $\langle u'w' \rangle$ are considered to identify dominant motions in the flow. The contribution is calculated as

$$S_i = \frac{\sum_{k=1}^N \langle u'w' \rangle_{i,k} I_i}{\sum_{k=1}^N \langle u'w' \rangle_k}, \quad (3)$$

where N is the total number of events observed for all quadrants, i is the quadrant of interest ($i = 1, 2, 3, 4$), k is the event number, and $I_i = 1$ if $\langle u'w' \rangle$ is located in the quadrant of interest and $I_i = 0$, otherwise.

2.2.1 Extension of Analysis through Time-Duration and Impulse

A recent study conducted by Bristow et al. (2021) extended the quadrant analysis over a barchan dune, by quantifying an average time-duration, T_Q , and average impulse strength, J_Q , for a quadrant event. The spatial evolutions of J_Q and T_Q provide insights into the impact of IBL development on turbulence producing motions and the sediment transport. An average time-duration for quadrant events, as provided in Bristow et al. (2021), may be calculated using

$$T_Q(x, z) = \frac{1}{N} \left[\sum_{k=1}^N (B_{Q,k} - A_{Q,k}) \right]. \quad (4)$$

Here, Q is the quadrant number, and $A_{Q,k}$ and $B_{Q,k}$ are the start and end time, respectively, of an event. The average time-duration can be re-written in non-dimensional form as

$$T_Q^* = \frac{T_Q U_c}{H_c} \equiv \frac{T_Q U_\infty}{k_a}, \quad (5)$$

where U_c is a characteristic velocity and H_c is a characteristic length scale, that together form a characteristic duration H_c/U_c (Bristow et al., 2021). We select the free stream velocity, U_∞ , as our characteristic velocity, and the average dune height, k_a , from Gunn et al. (2021) as our characteristic length scale. The impulse of a quadrant event is taken as the integral of $\langle u'w' \rangle$ over the event duration, providing insight into the potential for sediment transport (Bristow et al., 2021). As in Bristow et al. (2021), this integral is found with

$$J_Q(x, z) = \frac{1}{N} \sum_{k=1}^N \left[\int_{A_{Q,k}}^{B_{Q,k}} \langle u'(x, z, t) w'(x, z, t) \rangle dt \right]. \quad (6)$$

J_Q can be written in a non-dimensional form using a characteristic duration (H_c/U_c), and a velocity magnitude (Bristow et al. (2021)). We use the same characteristic duration as before, and an average friction velocity over the dune field, $u_{\tau,02}$.

$$J_Q^* = \frac{J_Q U_c}{H_c u_\tau^2} \equiv \frac{J_Q U_\infty}{k_a u_{\tau,02}^2}. \quad (7)$$

3 Numerical Setup and Methods

The simulations employed in this study are the same as those in previous work by the authors (Cooke et al., 2024). These simulations provided a wealth of data allowing us to examine new quantities, and conduct a new analysis on the same flow. This study builds on some of our previous findings; specifically, the relation between the development of the IBL and the observed thickening of the Reynolds shear stress profile after the roughness transition. In this study we examine the turbulent motions that underpin the observed self similarity. We begin by describing in detail the solver used, the data we validate against, and the studies conducted to ensure the results are insensitive to domain dimensions and grid spacing.

3.1 Numerical Solver Details

We deploy the LES flow solver *CharLES*, from Cadence Design Systems (Cascade Technologies), to simulate a neutrally buoyant atmospheric boundary layer flow. *CharLES* is an unstructured grid, body-fitted, finite-volume flow solver that solves the filtered variable-density Navier-Stokes equations, in a low-Mach isentropic formulation (Ambo et al., 2020; Brès et al., 2023). The code uses a second-order central discretization in space, and a second-order implicit time-advancement scheme (Brès et al., 2023). It is written in C++ and uses message-passing-interface to allow for parallelization.

The streamwise, spanwise, and wall-normal directions are represented by x, y , and z , respectively, with instantaneous velocity directions U, V , and W (or u_1, u_2 , and u_3). The filtered equations of mass and momentum are given by

$$\frac{\partial \tilde{\rho}}{\partial t} + \frac{\partial \tilde{\rho} \tilde{u}_i}{\partial x_i} = 0, \quad (8)$$

$$\frac{\partial \tilde{\rho} \tilde{u}_i}{\partial t} + \frac{\partial \tilde{\rho} \tilde{u}_i \tilde{u}_j}{\partial x_j} = -\frac{\partial \tilde{p}}{\partial x_i} + \frac{\partial}{\partial x_j} \left[(\mu + \mu_{SGS}) \left(\frac{\partial \tilde{u}_j}{\partial x_i} + \frac{\partial \tilde{u}_i}{\partial x_j} - \frac{2}{3} \delta_{ij} \frac{\partial \tilde{u}_k}{\partial x_k} \right) \right]. \quad (9)$$

Here, $\tilde{\rho}$ is the density of the fluid, \tilde{p} is the pressure, μ is the dynamic viscosity of the fluid, and μ_{SGS} is the subgrid scale (SGS) viscosity. Filtered quantities are denoted with a $\tilde{\cdot}$. The filter width is set by the grid-spacing, Δ , with turbulent motions larger than Δ resolved, and those smaller parameterized with an SGS model. For the remainder of the paper, all quantities without $\tilde{\cdot}$ are assumed to be filtered. The static-coefficient Vreman SGS model is used to close the SGS viscosity: (Vreman, 2004),

$$\mu_{SGS} = \tilde{\rho} C_V \sqrt{\frac{B_\beta}{\alpha_{ij} \alpha_{ij}}}, \quad (10)$$

where C_V is the Vreman coefficient, α_{ij} is the filtered velocity gradient, and B_β is the second invariant of $\beta_{ij} = \Delta^2 \alpha_{ij} \alpha_{ij}$. The low-Mach equation of state is given by

$$\tilde{\rho} = \frac{1}{c^2} (\tilde{p} - p_{ref}) + \rho_{ref}, \quad (11)$$

with the reference pressure and density, p_{ref} and ρ_{ref} , respectively, and speed of sound of the fluid, c . In assuming an isentropic approximation of the flow, the formulation provides the benefits of a variable density, compressible solver, while also removing the time-step restriction associated with low-Mach flows (Brès et al., 2023), which are common to ABL flows (Y. Hwang & Górlé, 2022). For describing statistical quantities, the instantaneous velocity (e.g., U) is decomposed into its time-averaged ($\langle U \rangle$) and fluctuating (u' ; about the mean) component: $U(x, y, z, t) = \langle U \rangle(x, y, z) + u'(x, y, z, t)$.

CharLES uses an isotropic Voronoi meshing scheme, which provides means to generate a highly scalable, high-quality body-fitted mesh, suitable for complex, irregular geometries (Y. Hwang & Górlé, 2022; Cooke et al., 2023; Brès et al., 2023; Y. Hwang & Górlé, 2023). The mesh generation is fully parallelized and automated, allowing for production of a grid with O(10M) elements in O(1) minutes using tens of processors. For mesh generation, a far-field grid spacing is first specified, Δ_{FF} , where this relative length-scale sets the refinement. Subsequent mesh spacing is then determined by $\Delta_{FF}/2^n$, where n is the desired number of refinement levels. More details of the Voronoi meshing technique are provided in Brès et al. (2023).

3.2 White Sands Field Data

We investigate the smooth-to-rough surface transition found at White Sands National Park (Fig. 1a). The field data from White Sands included in this study have been extensively described in prior works (Gunn et al., 2020, 2021; Cooke et al., 2024), and are briefly summarized here. Open-source topographic data (US Geological Survey, 2020) for White Sands were gridded at 1 meter spatial (x - y) resolution, with vertical (z) resolution of ~ 0.1 m (Gunn et al., 2020). The topography begins as a smooth playa surface (at $x = 0$ m), known as the Alkali Flat, and begins to rise into a roughness transition region (at $x \approx 1.8$ km), where dunes form as low-amplitude (~ 10 cm) sand waves with a fundamental wavelength ~ 20 m (Gadal et al., 2021). Large transverse dunes abruptly emerge (at $x \approx 1.9$ km) and, around a kilometer after the transition, the transverse dunes break into isolated, heterogeneous barchan dunes whose migration rate and peak height decline gradually over several kilometers, after which the dunes are eventually immobilized by vegetation (Jerolmack et al., 2012; Reitz et al., 2010; Lee et al., 2019).

The average dune height across the dune field from prior studies was found to be $k_a = 3$ m (Gunn et al., 2020, 2021). Because dune topography is spatially variable, however, we determine a spanwise-averaged dune elevation (in reference to the Alkali Flat $z = 0$ m in the numerical domain) and the root-mean-square (rms) of this elevation, presented against a center line profile in Figure 1b. Half kilometer bins of the dune field ($\hat{x} = 0 - 6$ km) are created to determine a localized \hat{k}_a and root-mean-square, \hat{k}_{rms} . Looking to Table 1, \hat{k}_a increases over the first kilometer (Bins 1 and 2), reaching a maximum between 2 - 3.5 km (Bins 3-5), then irregularly decreases over the remaining ≈ 3 km of the dune field (Bins 6-12). This behavior follows previously recorded and observed trends in dune height (Jerolmack et al., 2012), sediment flux (Gunn et al., 2020), and boundary stress (Cooke et al., 2024).

Table 1. Half kilometer bins of the spanwise-averaged dune height and dune height root-mean-square at that streamwise location. Average heights are relative to the Alkali Flat ($z = 0$ m). Corresponding bins for each streamwise probing stations are also indicated.

Bin	\hat{x} Stations	\hat{k}_a [m]	\hat{k}_{rms} [m]
1	\hat{x}_1 and \hat{x}_2	5.3980	1.2508
2	\hat{x}_3	7.5215	2.3894
3	\hat{x}_4	10.4724	2.1155
4	\hat{x}_5	9.8482	2.3725
5	\hat{x}_6	10.1459	3.2984
6	\hat{x}_7	9.2489	2.2941
7		9.5107	1.5359
8	\hat{x}_8	9.1641	1.6165
9		8.3660	0.9759
10	\hat{x}_9	8.3996	1.0459
11		8.2047	0.8953
12		8.2867	1.2080

We use flow velocity data from the Field Aeolian Transport Events (FATE) campaign, which, using light detecting and ranging (LiDAR) equipment, collected horizontal and vertical velocity data from two fixed x positions (Gunn et al., 2021), shown in Figure 1a. The LiDAR deployed in the study was a Campbell Scientific ZephIR 300 wind LiDAR velocimeter. Initially, the equipment was placed on the Alkali Flat upwind of the dune field, where it collected vertical velocity profiles every 17 seconds over approximately

70 days during the spring windy season of 2017 at White Sands. A year later, on the stoss side of a downstream dune, the LiDAR collected vertical velocity profiles every 17 seconds over approximately 25 days during the same windy season in 2018 at White Sands. Data were collected with a vertical resolution of 10 log-spaced bins, from $z = 10$ m to $z = 300$ m above the surface, with an additional point at $z = 36$ m. In their study, Gunn et al. (2021) found that, due to stratification effects, night-time winds produce a nocturnal jet that skims over a surface layer of cool stagnant air, which reduces boundary roughness effects and sediment transport. In order to remove the effects of buoyancy, which have been shown to be important for desert environments such as White Sands (Gunn et al., 2021), we isolate the effects of roughness by using only daytime measurements – the twelve hour window from 06:00 to 18:00 local time. The velocity within this window is then time-averaged to produce a daytime profile, and this process is completed for both the upstream and downstream LiDAR data. The upstream profile is first used to derive the inflow conditions to the simulation, and later as validation for the inflow portion of the LES calculation. Additionally, we validate the flow within the dune field with the downstream LiDAR data, which has also been averaged over the same twelve hour window described above.

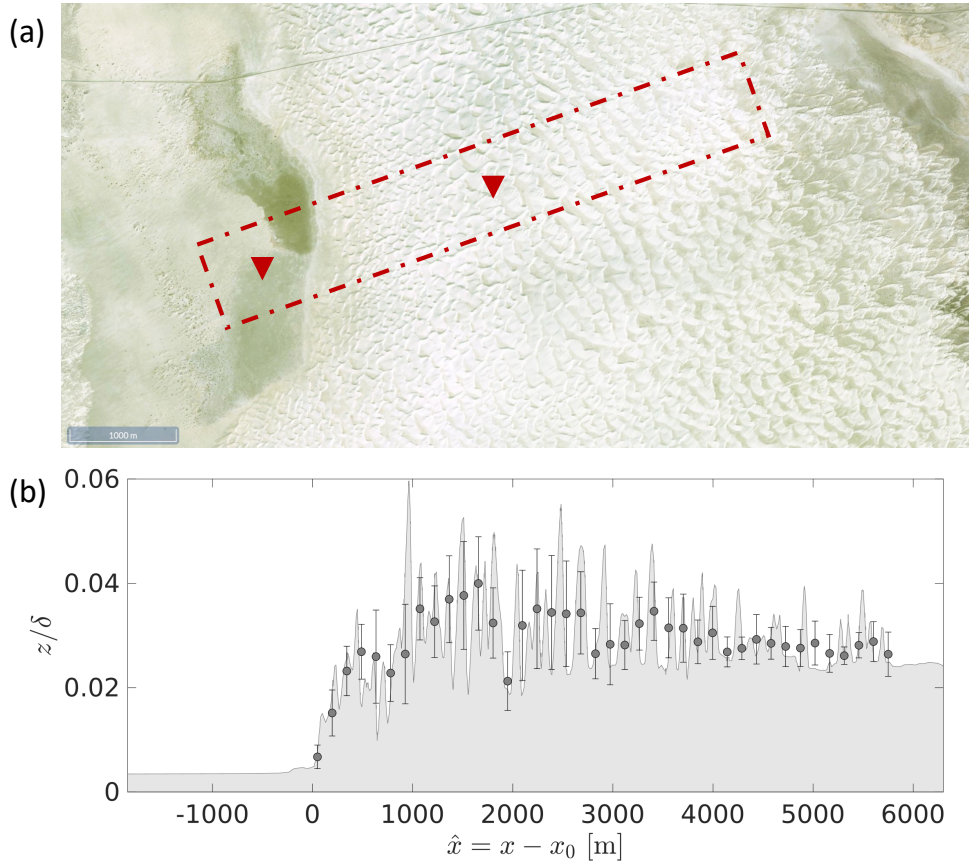


Figure 1. Field setting at White Sands dune field. (a) Satellite image of White Sands National Park, with the computational domain (red dot-dashed box) and two LiDAR observation stations (red triangles) marked. Flow is aligned with the dune formation direction. (b) A center line profile of the dune field in the numerical study (shaded area), featuring spanwise-averaged dune heights (gray circles), and their root-mean-square of the dunes along the span at each streamwise location (bars markers). All wall-normal elevations are normalized by $\delta = 300$ m.

3.3 Computational Domain and Validation

We numerically analyze a neutrally-buoyant statistically steady ABL flow over an 8.6- by 0.5-km domain of the White Sands topographic data, depicted in Figure 2, oriented in the direction of dominant winds and dune migration (~ 15 degrees N of E). The domain length is set to capture the mesoscopic scale of the IBL development, $\sim 30\delta$, where δ is the ABL height. Similarly, the width, determined in the sensitivity study outlined in Section 3.3.1, is much larger than an individual dune. At White Sands, prior observations of δ have estimated the thickness to fluctuate daily between $O(10^2-10^3)$ m (Gunn et al., 2020, 2021). We choose the height of the domain, h , to be $h = 1000$ m. The height of the ABL is chosen to be $\delta = 300$ m, as this is the height of the highest data collection point in the FATE campaign, preventing validation above this elevation, and it lies near the midpoint of the previously observed range at White Sands. For the top and side-walls of the domain, we employ a symmetry boundary condition. At the inflow, a synthetic inflow generation based on digital filter techniques is implemented (Klein et al., 2003), which has been previously used in non-equilibrium WMLES studies (Hu et al., 2023; Hayat & Park, 2023; Cooke et al., 2024). At the outflow a numerical sponge is deployed to minimize numerical effects (Mani, 2012; Bodony, 2006), and the end of the domain is extended to establish a sponge zone that does not influence the study. On the Alkali Flat and the dune field, we employ the algebraic (equilibrium) wall-model (Bodart & Larsson, 2011; Kawai & Larsson, 2012), derived from the simplified boundary layer equations which assumes only the wall-normal diffusion.

We extend the numerical domain of the Alkali Flat to first ensure the inflow profile becomes a fully-developed, zero-pressure-gradient turbulent boundary layer (ZPG TBL), before encountering the roughness transition. As a check we examine the evolution of the skin-friction coefficient C_f against the momentum thickness Reynolds number Re_θ . As seen in Figure 3a, C_f converges towards the empirical correlation for a ZPG TBL, well before the roughness transition, giving confidence to the inflow development. Additionally, low-speed streaks closest to the wall are shown to have lengths of about $2\delta_0 - 3\delta_0$, where $\delta_0 \approx 30$ m is the Atmospheric Surface Layer (ASL) height, further matching what would be expected of fully developed turbulent flow (J. Hwang et al., 2016). As a test of validity for our model, we compare the time-averaged horizontal velocity profile of our simulation to the observations of FATE on the Alkali Flat, presented in Figure 3b. The values from the simulation agree within 5% error compared to the observed values. Considering that the field data are averaged over a non-stationary forcing, and that buoyancy effects are not included in the simulation, this agreement is remarkable, indicating that treatment of the ABL flow at White Sands as steady and neutrally buoyant is an appropriate model.

The mesh deployed in the study contained approximately 85×10^6 control volumes, and used $\Delta_{FF} = 28$ m with five levels of refinement, yielding a minimum grid-spacing $\Delta_{min} = 0.75$ m closest to the surface. We note that despite the refinement leading to the average dune height being resolved by four control volumes, in viscous units our near-wall spacing is $\Delta_{min}^+ \approx 3200$, due to the high Re_τ . Here, \cdot^+ denotes scaling with viscous units, $\delta_\nu \equiv \nu/u_\tau$ and u_τ . However, we adequately resolve the ABL height with ≈ 67 control volumes, as well as the IBL with a minimum of ≈ 20 and a maximum of ≈ 46 , over the course of its development. We next justify our mesh choice with a grid sensitivity study.

3.3.1 Domain and Grid Sensitivity Studies

A parametric study was conducted to ensure the finite spanwise domain size along with the use of a symmetry boundary condition on the spanwise boundaries had no influence on quantities of interest along the center line. Three domains with constant streamwise length and wall-normal height were tested with three varying spanwise widths. An

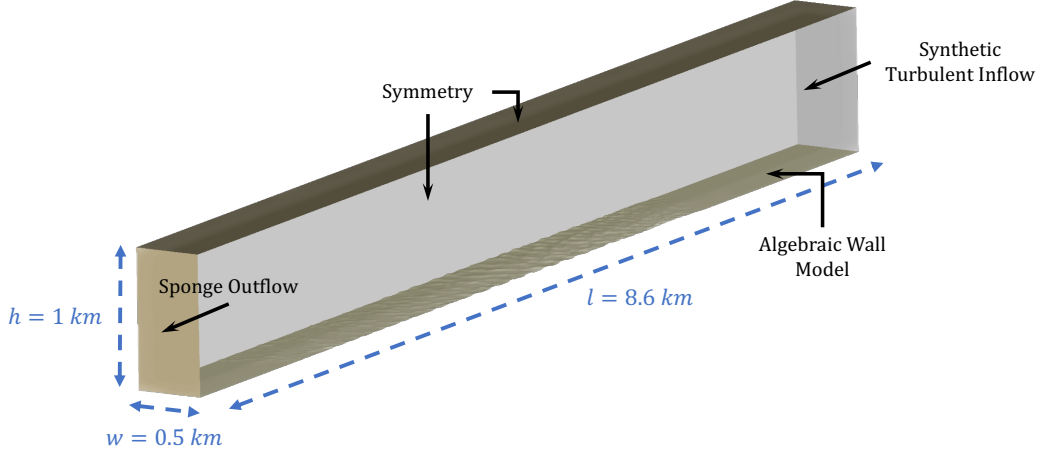


Figure 2. Simulation domain setup. A synthetic turbulent inflow boundary condition is imposed at the inlet, a numerical sponge is used at the outlet, the top and side walls deploy a slip boundary condition, and an algebraic wall-model is applied to the bottom surface, which is the scan of the dune field topography. The domain is 8.6 km in streamwise length, 0.5 km in spanwise width, and 1 km in height.

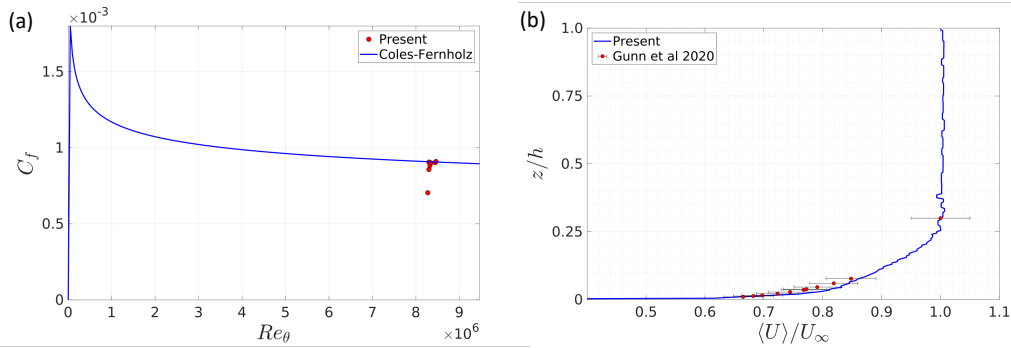


Figure 3. Inflow boundary condition characterization and validation. (a) Comparison of our simulated skin-friction coefficient as a function of Re_θ (black, red-filled circles) – at multiple streamwise locations upstream of the roughness transition – against the Coles-Fernholz correlation for Re_θ (Fernholz & Finley, 1996) (blue line). (b) Validation of $\langle U \rangle$ from a coarse LES calculation (blue line) against the FATE campaign data (Gunn et al., 2021) (black, red-filled squares) with error bars showing $\pm 5\%$. Values from the simulation are normalized by U_∞ from the simulation, whereas values from the field campaign are normalized with an experimental U_∞ .

initial width of 500 m was chosen as the baseline, denoted by L_y , followed by domains with spanwise lengths $1.5L_y$ and $2L_y$. The center line mean-flow quantities and boundary stress values were compared for each of the three domains to determine the effect of the domain span. Downstream of the roughness transition, we probe at ten logarithmically-spaced stations. For brevity we only show four locations when comparing values in the study. Some of the probing stations are on the stoss (upwind) side and others on the leeward (downwind) side of a dune, but this has no effect on study results. At present, we find minimal difference in values of interest along the center line with varying domain

width in the spanwise direction. The mean streamwise velocity profiles obtained with different domain sizes, shown in Figure 4a-d, are nearly identical and overlapping with each other at all stations. The evolution of τ_b , an important parameter for sediment transport, was examined next in non-dimensional form using C_f (Fig. 4e); as was the case with $\langle U \rangle$, it remains mostly unchanged. Minor sensitivities to the domain size towards the downstream end of the dune field are seen vanishing on the two larger domain sizes. Overall, there is minimal variation between the span lengths, and the same center line trends are captured. For the present investigation, due to the added costs of larger domains and the minimal changes to the quantities of interest, we have kept $L_y = 500$ m as the spanwise width.

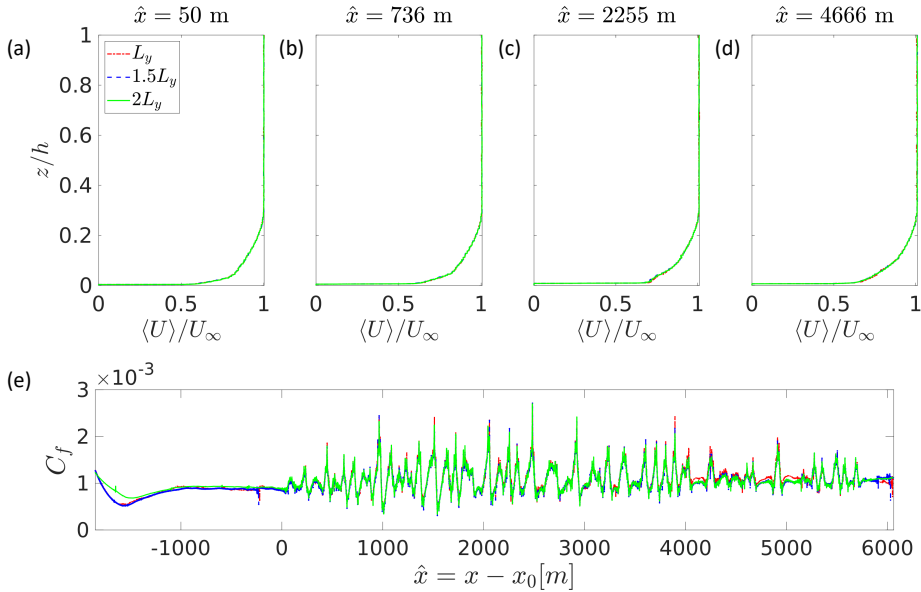


Figure 4. Insensitivity of results to domain width. (a) Normalized mean streamwise velocity, $\langle U \rangle / U_\infty$, at $\hat{x} = 50$ m for L_y (red dot-dashed line), $1.5L_y$ (blue dashed line), and $2L_y$ (green solid line). (b) $\langle U \rangle / U_\infty$ at $\hat{x} = 736$ m, (c) at $\hat{x} = 2255$ m, and (d) at $\hat{x} = 4666$ m, colors and line styles are the same as (a). (e) Magnitude of the mean skin-friction coefficient ($C_f = \langle \tau_b \rangle / (0.5\rho U_\infty^2)$) at the center line; colors and line styles are the same as (a).

An additional study was completed to ensure grid convergence. After iterative choices for mesh design were completed, two meshes with varying near-wall resolution were tested, both having the same structure. Details of the two meshes are given in Table 2.

Table 2. Details of the coarse and fine meshes deployed in the grid sensitivity study. Presented are the far-field and minimum grid spacings, the minimum grid spacing in viscous units, and the total number of control volumes.

Mesh	Δ_{FF} [m]	Δ_{min} [m]	Δ_{min}^+	Total CVs [Millions]
Coarse	38.0	1.0	4375	46.5
Fine	28.0	0.75	3200	85.4

The mean streamwise velocity is nearly unchanged between the two grids (Fig. 5a-d). Similarly, the center line value of C_f is mostly unaffected by the choice of mesh resolution (Fig. 5e). Minor differences do exist upstream near the computational inlet; however, this only has a small effect on the inflow turbulence development rate. For this investigation, we deploy the finer of the two meshes.

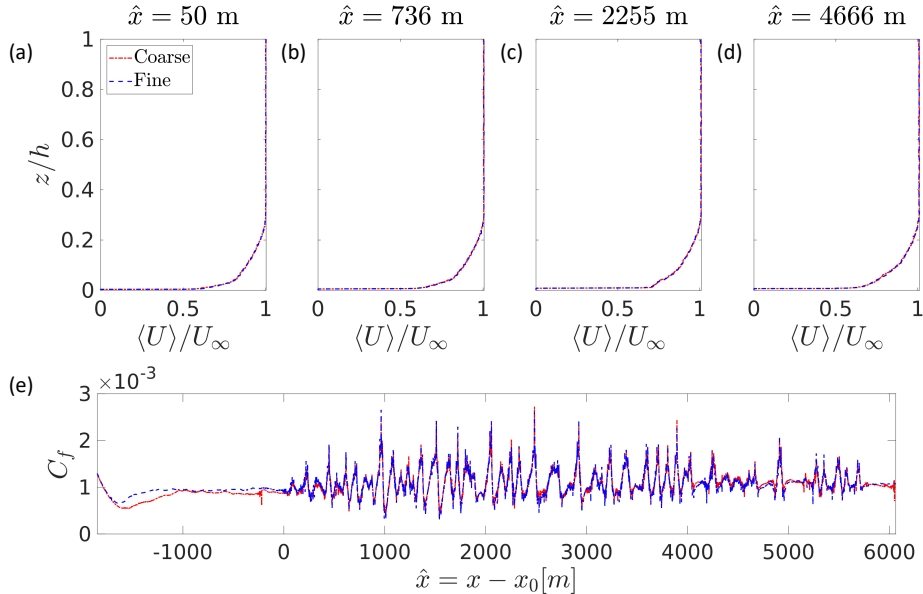


Figure 5. Insensitivity of results to mesh resolution. (a) Normalized mean streamwise velocity, $\langle U \rangle / U_\infty$, at $\hat{x} = 50$ m for the Coarse (red dot-dashed line) and Fine (blue dashed line) meshes. (b) $\langle U \rangle / U_\infty$ at $\hat{x} = 736$ m, (c) at $\hat{x} = 2255$ m, and (d) at $\hat{x} = 4666$ m, colors and line styles are the same as (a). (e) Magnitude of the mean skin-friction coefficient at the center line; colors and line styles are the same as (a).

4 Results

4.1 IBL Development and Turbulence Within

We briefly summarize the key findings of our prior work (Cooke et al., 2024) that are relevant to the study described herein. We first calculate the δ_i downstream of the roughness transition using Equation 2, at ten streamwise log-spaced stations from $\hat{x}_1 = 50$ m to $\hat{x}_{10} = 5751$ m (Fig. 6a). Wall-normal elevations are probed at equal intervals, between 0–400 m, for $\langle u'u' \rangle$. We use the mean velocity at $z = 400$ m – which is well outside the ABL – for U_∞ and δ to normalize \hat{x} .

A correlation of the form given in Equation 1 is fit to the data, and we use $z_{02} = 10^{-1}$ m, found by Gunn et al. (2020, 2021) in the FATE campaign. We find the coefficient $a = 0.29$ and the exponent $b = 0.71$. Our correlation from the determined values of δ_i has good agreement with classic scaling models (Elliott, 1958; Townsend, 1965; Antonia & Luxton, 1972a; Wood, 1982; Pendergrass & Aria, 1984; Savelyev & Taylor, 2001). Additionally, our power-law value, b , agrees well with M. Li et al. (2021); using this method, they found values of $a = 0.75$ and $b = 0.77$ for their two datasets in their rough-to-smooth transition study.

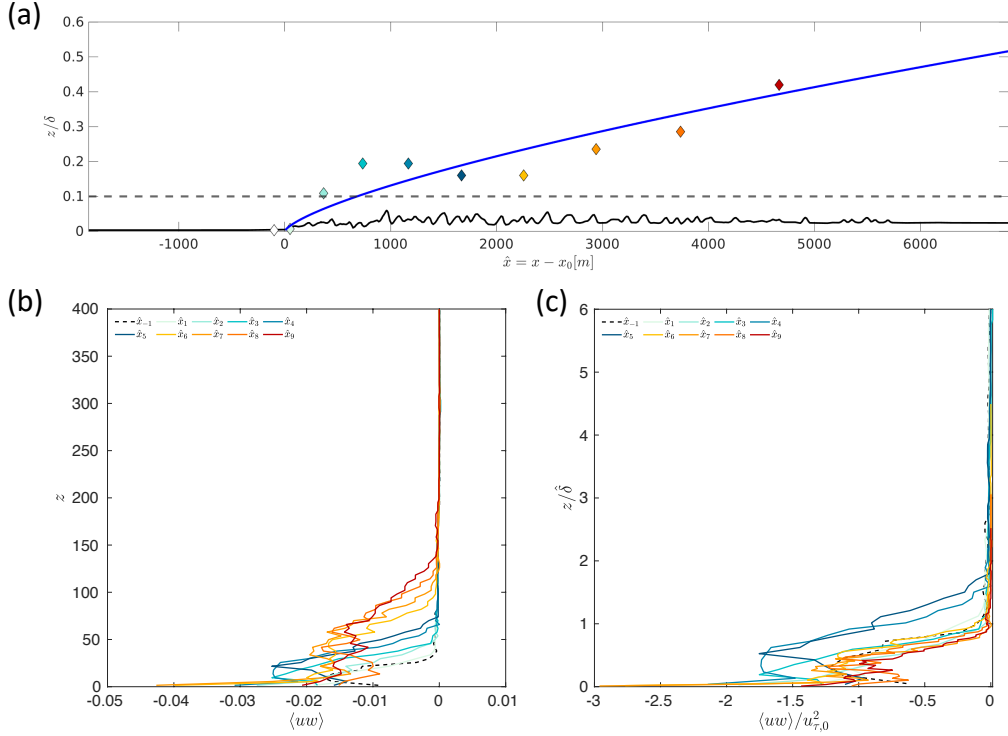


Figure 6. Summary of results from Cooke et al. (2024). (a) Calculated IBL height (multi-colored diamonds) along the center line of the dune field (black line). A correlation (blue line) for the data is found to be $\delta_i/z_{02} = 0.29(\hat{x}/z_{02})^{0.71}$, where $z_{02} = 10^{-1}$ m (Gunn et al., 2020, 2021). (b) Reynolds shear stress profiles downstream of the roughness transition. Within the dune field, locations correspond to diamonds with matching colors in (a). A profile upstream of the roughness transition in the Alkali Flat (white diamond in (a)) is included as a dashed black line. (c) The same profiles as in (b) normalized with $u_{\tau,02}$, and plotted against $z/\hat{\delta}$. Here, $\hat{\delta} \equiv \delta_0 = 30$ m for the data found in the Alkali Flat and at the first station, \hat{x}_1 ; otherwise $\hat{\delta} \equiv \delta_i$ (local IBL height) for all other downstream stations. Colors and line styles are the same as (b). We see that most profiles collapse onto a master curve.

We note that the correlation is constructed with an assumed homogeneous roughness parameter governing the whole dune field. Looking at Table 1, we see there is significant variability in \hat{k}_a over the first few kilometers. Over the first kilometer of the dune field, relatively low amplitude dunes are superimposed on a topographic ramp. Beyond this ramp, dunes grow in size while the underlying topography levels out (Fig. 1b). Thus, the flow may actually experience two roughness transitions; first, from the smooth Alkali Flat to the low-lying transverse dunes, and second from the low-lying dunes to the larger isolated barchan dunes. Looking to Figure 6a, the simulated IBL heights are suggestive of two transitions – or, at least, the IBL height exhibits long-wavelength fluctuations. Nevertheless, assuming homogeneity in roughness captures the first-order growth of the IBL.

In Figure 6(b), profiles of the Reynolds shear stress $\langle u'w' \rangle$ after the roughness transition reveal a noticeable thickening downstream. Our prior work (Cooke et al., 2024) found a reasonable collapse of these profiles when z is normalized by the relevant length-scale, $\hat{\delta}$, indicating a self-similarity of the turbulence within the IBL. This observed col-

lapse is given in Figure 6c. Here, $\hat{\delta} \equiv \delta_0 = 30$ m for the data in the Alkali Flat and at the first station, \hat{x}_1 . For these first two locations, the ASL is the relevant length-scale. By at \hat{x}_2 , δ_i grows larger than δ_0 , and hence $\hat{\delta} \equiv \delta_i$ is chosen as the relevant length-scale.

The past work in Cooke et al. (2024) also investigated changes to the interaction between the large-scale and small-scale motions of the flow. It was shown with R_{AM} that the negative peak associated with the anti-correlation of the scale interaction shifted further from the wall with increasing \hat{x} . When plotting R_{AM} against $z/\hat{\delta}$, the location of the negative peak for each streamwise location collapsed to a similar point within the IBL ($z/\hat{\delta} \approx 0.5$). Due to the proximity of the peak near the outer portion of the IBL it was believed that this negative peak corresponded to the intermittency associated with the edge of the IBL and the ABL. We present these previous results to frame the study of interest: how do turbulence producing motions evolve downstream of the roughness transition, and why is δ_i the critical length-scale for these flows?

4.2 The Role of δ_i in Turbulence within the IBL

As outlined in Section 2.2, turbulent momentum transport associated with $\langle u'w' \rangle$, and may be quantified through quadrant analysis. We plot u' and w' in the Alkali Flat and downstream in the dune field, at three wall-normal elevations: $z/\delta = 0.06, 0.1$ and 0.3 (Fig. 7). In the smooth Alkali Flat, we observe that the closest wall-normal location behaves as expected in typical ZPG TBLs (Fig. 7a). A majority of the points are located within the second and fourth quadrants, which represent the turbulence-producing ejection and sweep events, respectively. Moving away from the wall, the turbulence within the atmospheric surface layer is expected to gradually decrease. Indeed, at $z/\delta = 0.1$ the magnitude of the fluctuations is seen to decrease, with fewer points residing in Q_2 and Q_4 . Furthest from the wall, the fluctuating velocity magnitude is diminished, and the frequency of each motion is nearly indistinguishable; i.e., there is no observable preference for any quadrant.

Downstream of the roughness transition, the results from the lowest elevation remain largely unchanged (Fig. 7b-j). Similarly, the results at $z/\delta = 0.1$ and 0.3 at the first station (Fig. 7b) closely resemble those of the Alkali Flat, as the relevant length-scale is still δ_0 here. However, we begin to see changes to these wall-normal elevations as we move further downstream, and δ_i grows larger than δ_0 . For $z/\delta = 0.1$, the change is almost immediate, as $\delta_i > \delta_0$ by \hat{x}_2 (Fig. 7c). This is reflected by both an increase in the magnitude of the velocity fluctuations, and in the number of events in Q_2 and Q_4 . By \hat{x}_5 (Fig. 7g), the magnitude of the fluctuations at $z/\delta = 0.1$ matches those found at $z/\delta = 0.06$, and the frequency of sweep and ejection events is nearly equivalent; this behavior is maintained downstream. Furthest from the wall, we observe almost no change in magnitude or frequency from the Alkali Flat, reflecting the dissipation of the Reynolds shear stress, and subsequently, the turbulent motions, further from the wall beyond δ_0 . However, at \hat{x}_7 (Fig. 7h), there is a clear change to the flow, as the IBL height is nearing $z/\delta = 0.3$; this is evident from the increase in both magnitude and frequency of ejection events. At the next two streamwise locations this trend continues, with increasing frequency and magnitude of turbulence-producing ejection events (Figs. 7i, 7j). The enhancement of ejection events is associated with δ_i growing beyond $z/\delta = 0.3$. The upshot of these observations is this: as the IBL thickens downwind, regions of the flow that are subsumed by it exhibit increased turbulence producing motions.

With Equation 3, we quantify the contributions to the Reynolds shear stress by each quadrant, S_i , and observe the changes occurring downstream of roughness transition. In the Alkali Flat (Fig. 8a) closest to the surface, the majority of the contributions to $\langle u'w' \rangle$ come from Q_4 events. Farther from the wall, however, Q_2 motions become the highest contributor and Q_4 contributions correspondingly decrease. At $\approx z/\delta = 0.1 \equiv \delta_0$ the

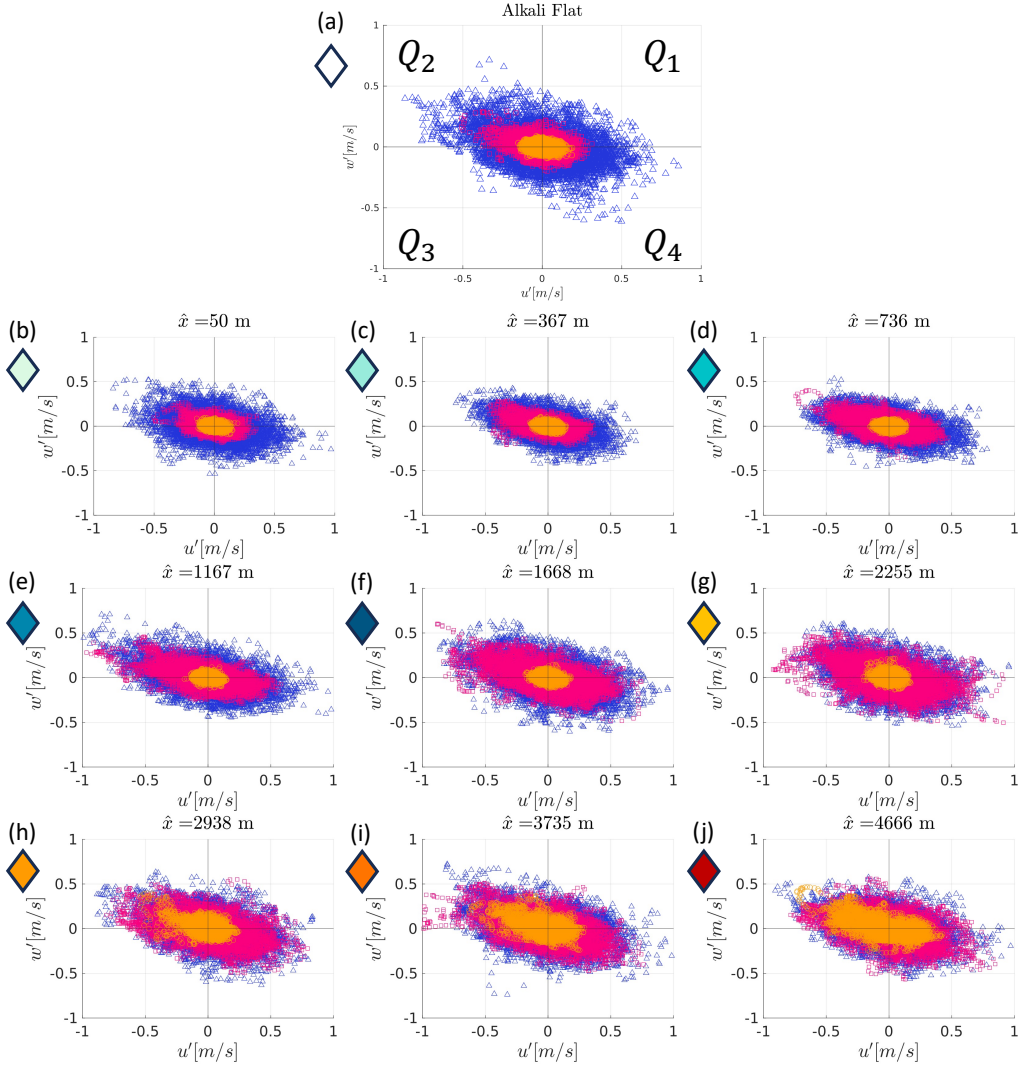


Figure 7. Quadrant analysis of turbulence at three relative bed heights, for ten downstream probing stations. Diamond colors correspond to the location within the dune field and IBL height from Figure 6a. (a) Scatter plot of the product of the streamwise and wall-normal velocity fluctuations, u' and w' , respectively, in the Alkali Flat. Here, we see healthy turbulence at the lowest wall-normal elevation $z/\delta = 0.06$, represented by the purple triangles, where a majority of the motions reside in the second (upper left) and fourth (lower right) quadrants. At the second highest elevation at $z/\delta = 0.1$, given by pink squares, we expect to see lower magnitudes of the fluctuations, and a decrease in frequency of motions in the Q_2 and Q_4 as turbulence decays further from the wall. At the highest elevation, $z/\delta = 0.3$ given by orange circles, we expect to see lower magnitudes of fluctuations, and no preference for Q_2 and Q_4 . (b-j) Same plots as (a), at stations downstream of the roughness transition. Magnitude of fluctuations, and the frequency of Q_2 and Q_4 motions, at $z/\delta = 0.1$ increases with streamwise distance beginning at (c). For $z/\delta = 0.3$, these quantities begin to increase at (h). Overall, we see an increase in the magnitude and frequency of turbulence producing motions away from the wall, as the IBL grows to subsume these higher elevations.

contributions from Q_2 and Q_4 events become nearly equivalent. By $\approx z/\delta = 0.6$, all quadrant motions have approximately equal contribution. The trends are similar at \hat{x}_1 (Fig. 8b). We see a change beginning at the second IBL station \hat{x}_2 (Fig. 8c), where the local spike in Q_2 contributions (and corresponding dip in Q_4 contributions) moves farther from the wall. As we continue to move downstream, the associated spike (and dip) systematically moves to higher relative heights above the wall. there is an increase in distance from the surface where the Q_2 contribution peaks. This corresponds as well to a distance further from the wall where contributions from Q_2 and Q_4 events becomes nearly equal again. This perceived trend continues downstream, where the Q_2 and Q_4 contributions are initially similar, then diverge with peak contributions from Q_2 motions occurring further from the wall with increasing \hat{x} .

To uncover the downstream evolution of the length- and time-scales in the flow, we examine changes to the energy frequency spectrum of the the streamwise velocity fluctuations, $E(\omega)$ (Fig. 9). We take the long time-series data at four wall-normal elevations: $z/\delta = 0.01, 0.06, 0.1$, and 0.3 and transform the data into the frequency domain using the Fourier transform, in order to compute $E(\omega)$. Further details of this process are given in (Park & Moin, 2016). Upwind of the dune field, $E(\omega)$ in the Alkali Flat (Fig. 9a) demonstrates the reduction in turbulence further from the wall, as the energy contained in the flow at all frequencies decreases. This trend is seen at \hat{x}_1 as well (Fig. 9b). By \hat{x}_1 (Fig. 9c), there is an observed increase in the energy contained at lower frequencies (larger scales) for $z/\delta = 0.06$ and 0.1 , such that their magnitudes are nearly equal. This observation is another sign of the influence of IBL growth; as δ_i grows to subsume these elevations, we see an increase in large-scale turbulence. Further from the wall, at $z/\delta = 0.3$, values of $E(\omega)$ remain lower and unchanged as the IBL height has yet to reach this height. By \hat{x}_7 (Fig. 9h) however, δ_i approaches $z/\delta = 0.3$, and we see the energy associated with long time-scales begin to increase. By \hat{x}_9 (Fig. 9j), the energy at all elevations for lower frequency turbulence is roughly equal. Within the dune field, we can compute the expected frequency of turbulent motions (using the frozen turbulence hypothesis) associated with the the scale of the IBL using $\omega = U_c/\hat{\delta}$, where $U_c \equiv \langle U \rangle(z = \hat{\delta})$. With increasing downstream distance, the computed frequency associated with IBL-scale turbulence decreases. This computed frequency also corresponds roughly with the scaling break in the energy frequency spectrum, which is typically associated with the turnover time of the largest-scale eddies in the system. Taken together, results suggest that the developing IBL sets the scales of large-scale turbulence within it.

4.3 Evolution of T_Q and J_Q

We now focus on changes to the strength and time-duration for all quadrant events, with an emphasis on ejections and sweeps, after the roughness transition. We use Equations 4 and 6 to examine how turbulence producing motions evolve after the roughness transition. We collect time-series data for over 50 large-eddy turnover times, $T \equiv \delta/U_\infty$, resulting in $\sim O(10^3)$ separate quadrant events detected at each elevation and streamwise location. We record events at all streamwise stations in the dune field up to $z/\delta = 1.33$, and will focus on four elevations: $z/\delta = 0.01, 0.06, 0.1$, and 0.3 . We include data at the Alkali Flat to provide a baseline to compare against. As was done by Bristow et al. (2021), we do not filter events to prevent loss of long-time quadrant events that have smaller magnitudes.

To understand changes to the frequency of events in the streamwise direction at each elevation, we take the ratio of the number of events in one quadrant to the total number of events in all quadrants (Fig. 10). Nearest the surface at $z/\delta = 0.01$ (Fig. 10a), the frequency of events looks as expected in both the Alkali Flat and the dune field, with a majority of the events being ejections and sweeps. Looking first at results for the Alkali Flat further from the wall, at $z/\delta = 0.06$ (Fig. 10b), there is a slight reduction in Q_2 and Q_4 events, and a concomitant increase in Q_1 and Q_3 events. At $z/\delta = 0.1$ (Fig. 10c)

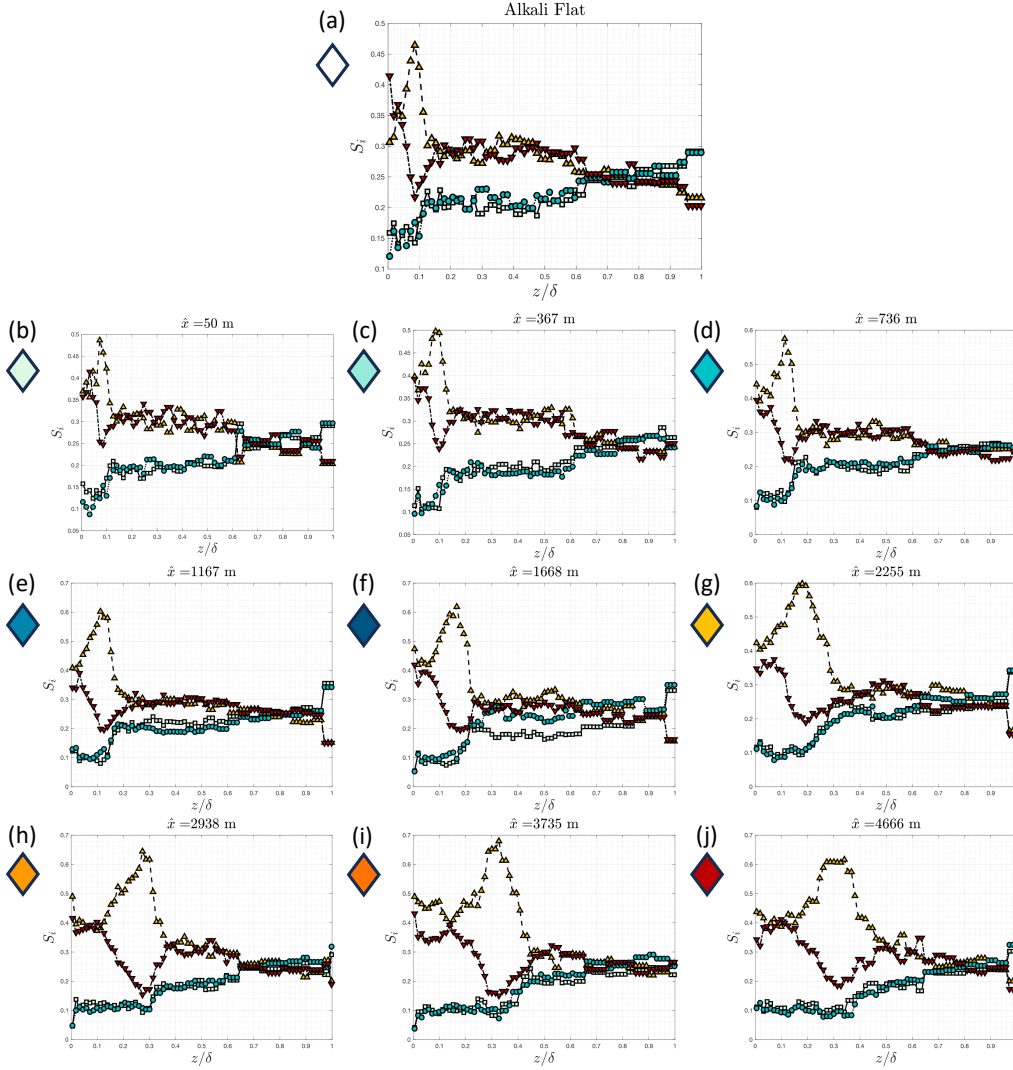


Figure 8. Contributions to the Reynolds shear stress, S_i , where $i = 1, 2, 3$, and 4 , corresponding to each quadrant. Diamond colors correspond to the location within the dune field and IBL height from Figure 6a. The green squares represent outward motions (Q_1), upward red triangles represent ejections (Q_2), blue circles represent inward motions (Q_3), and downward yellow triangles represent sweeps (Q_4). (a) The Alkali Flat station. Near the bed, Q_2 and Q_4 contributions are roughly equal. Farther from the wall the contribution from ejections increases, with a corresponding decrease in contribution from sweeps. Farther still the contributions become roughly equal again. (b) S_i at $\hat{x} = 50$ m, (c) $\hat{x} = 367$ m, (d) $\hat{x} = 736$ m, (e) $\hat{x} = 1167$ m, (f) $\hat{x} = 1668$ m, (g) $\hat{x} = 2255$ m, (h) $\hat{x} = 2938$ m, (i) $\hat{x} = 3735$ m, and (j) $\hat{x} = 4666$ m. We observe a systematic downstream increase in the distance from the wall where Q_2 and Q_4 motions contribute to $\langle u'w' \rangle$.

the frequencies of each event type change little from $z/\delta = 0.06$. However, farthest from the wall at $z/\delta = 0.3$ (Fig. 10d), we see the frequency of Q_1 and Q_3 events has increased, causing an additional decrease in Q_2 and Q_4 events. This is expected as the turbulence producing motions were seen to decrease away from the wall in the Alkali Flat (Fig. 7a). Focusing now on changes within the dune field, at the lowest elevation (Fig. 10a), there

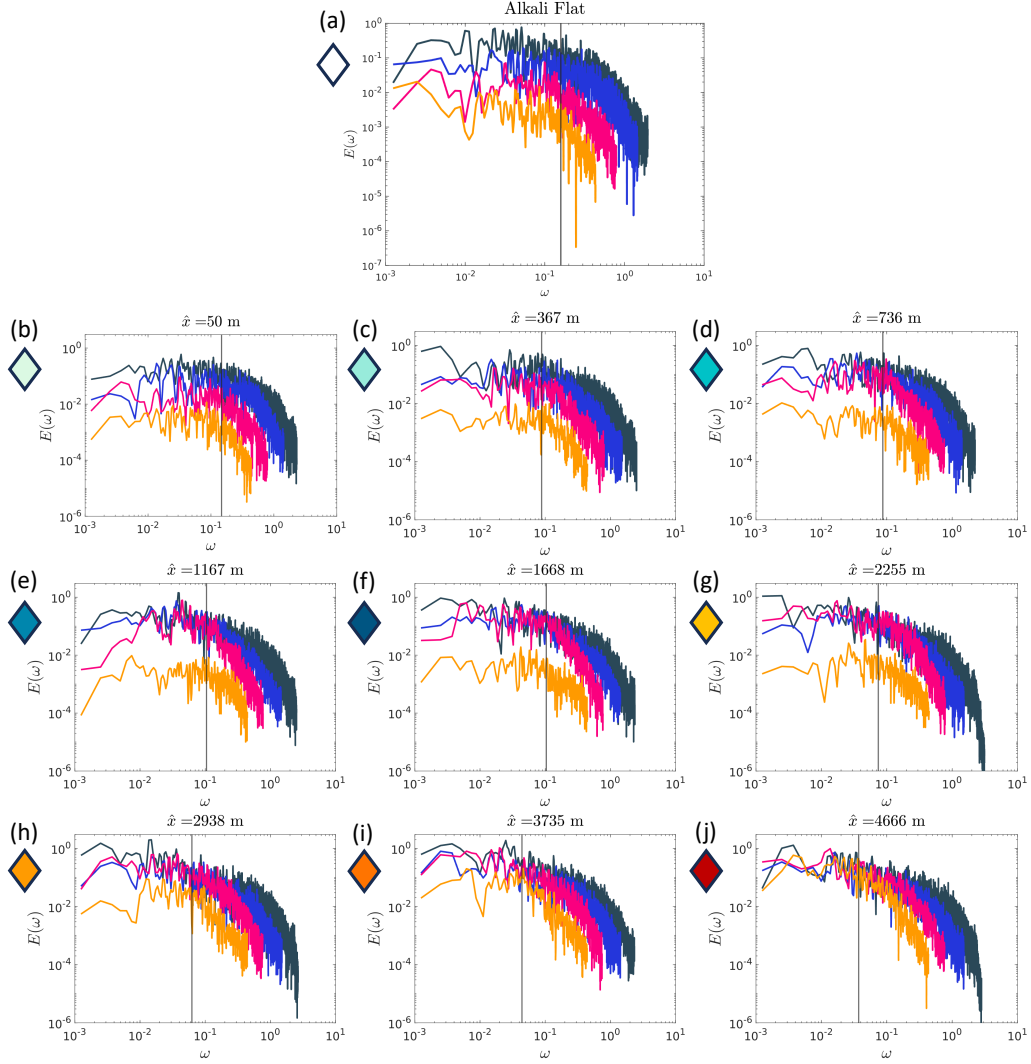


Figure 9. Energy frequency spectrum of the streamwise velocity fluctuation, $E(\omega)$, at four heights for the ten probing stations. The heights $z/\delta = 0.01, 0.06, 0.1,$ and 0.3 correspond to dark gray, purple, pink, and orange lines, respectively. Diamond colors correspond to the location within the dune field and IBL height from Figure 6a. Vertical black line represents the frequency associated with the eddy turnover time at the scale of the IBL, $\omega_i \equiv U_\infty(z=\hat{\delta})/\hat{\delta}$. This frequency decreases as the IBL thickness grows, and corresponds roughly to the scale break in the energy spectra. (a) Alkali Flat. $E(\omega)$ decreases with increasing distance from the wall, at all frequencies. (b) $E(\omega)$ at $\hat{x} = 50$ m, (c) $\hat{x} = 367$ m, (d) $\hat{x} = 736$ m, (e) $\hat{x} = 1167$ m, (f) $\hat{x} = 1668$ m, (g) $\hat{x} = 2255$ m, (h) $\hat{x} = 2938$ m, (i) $\hat{x} = 3735$ m, and (j) $\hat{x} = 4666$ m. We observe that as the IBL grows to subsume higher elevations, the magnitude of $E(\omega)$ for low-frequency turbulence grows. Note that once all elevations are within the IBL (j), the turbulent energy at low frequencies is the same for all elevations.

are subtle differences between \hat{x}_5 and \hat{x}_8 , where there is a definite reduction in the Q_1 and Q_3 events and concomitant increase in the frequency of Q_2 and Q_4 events. At $z/\delta = 0.06$ (Fig. 10b), we find at all \hat{x} that Q_2 and Q_4 events occur more frequently, although the highest (lowest) frequency of Q_2 and Q_4 (Q_1 and Q_3) events occurs between \hat{x}_4 to

\hat{x}_6 . At $z/\delta = 0.1$ (Fig. 10c), event frequency at \hat{x}_1 is similar to the Alkali Flat at the same elevation. There is a significant change, however, beginning at \hat{x}_2 . Since the IBL height has surpassed the ASL height, there is an observed increase in Q_2 and Q_4 event frequency, continuing for all other \hat{x} . Farthest from the wall (Fig. 10d), event frequency for all quadrants from \hat{x}_1 to \hat{x}_6 is similar to the Alkali Flat. Beginning at \hat{x}_7 , Q_4 event frequency increases, and continues to do so further downstream. We observe a concomitant decrease in Q_1 and Q_3 events at these stations. These observed changes in event frequency are due to the IBL height surpassing $z/\delta = 0.3$.

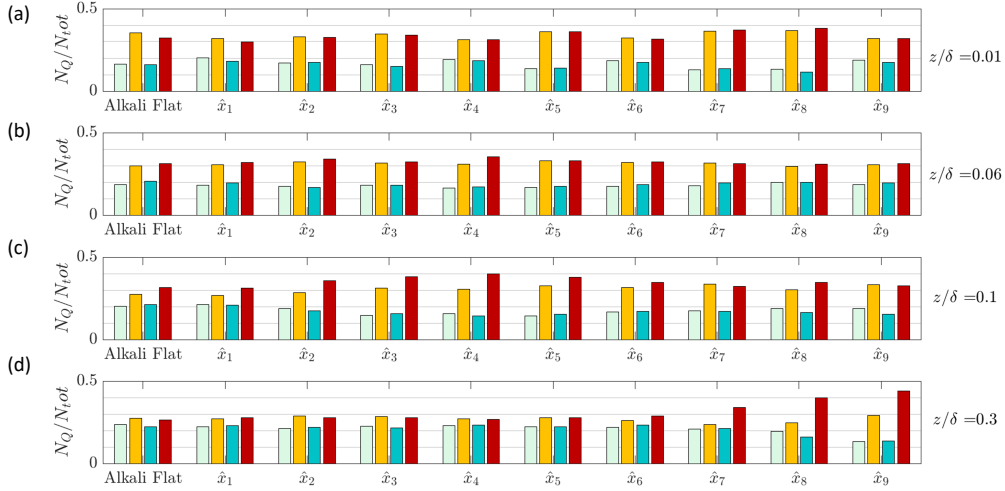


Figure 10. Relative frequency of quadrant events for each probing station, at distinct relative heights z/δ . Bars are in order of quadrant (left to right), with mint-green for Q_1 , yellow for Q_2 , blue for Q_3 , and red for Q_4 . (a) The lowest elevation z/δ . Behavior is as expected, with Q_2 and Q_4 events occurring most frequently. (b) $z/\delta = 0.06$, (c) $z/\delta = 0.1$, and (d) $z/\delta = 0.3$. Note the relative increase in Q_2 and Q_4 events at higher elevations moving downwind; as the IBL grows to subsume higher elevations, these turbulence producing motions increase.

We present the results of the average time-duration, T_Q , for each quadrant event, given in its non-dimensionalized form, T_Q^* (Equation 5). Results for the Alkali Flat and all \hat{x} in the dune field are presented in Figure 11. For calculating T_Q^* , we choose U_c to be U_∞ (as before $\langle U \rangle(z = 400 \text{ m})$), and k_a from the FATE campaign. We first observe changes in elevation at the Alkali Flat. Starting at $z/\delta = 0.01$ (Fig. 11a), we observe that Q_2 and Q_4 events are on average longer than Q_1 and Q_3 motions. For $z/\delta = 0.06$ (Fig. 11b), this pattern still holds; however, there is an increase in T_Q^* for all events, including Q_1 and Q_3 motions. This increase does not continue at higher elevations $z/\delta = 0.1$ and 0.3 (Figs. 11c and 11d); the opposite trend is observed, where T_Q^* is shown to decrease at higher elevations in the Alkali Flat. Within the dune field, the most distinctive pattern is that, for the two elevations closest to the wall (Figs. 11a and 11b), events corresponding to Q_2 and Q_4 are longer than those corresponding to Q_1 and Q_3 motions. Additionally, as was seen with the Alkali Flat, there is an increase in T_Q^* magnitude when moving away from the wall. We observe a similar pattern as was seen with the frequency in Figure 10b, where the longest average events occur at the point where they have the highest frequency at $z/\delta = 0.06$ (\hat{x}_4 to \hat{x}_6). For $z/\delta = 0.1$ (Fig. 11c), T_Q^* at \hat{x}_1 has nearly identical values to those in the Alkali Flat, but by \hat{x}_2 , there is a significant increase in T_Q^* , as the IBL height has surpassed the ASL height. This also holds for $z/\delta = 0.3$;

T_Q^* is similar at all \hat{x} locations to that in the Alkali Flat, until \hat{x}_7 , where the IBL height begins to surpass $z/\delta = 0.3$. Outside of the IBL, T_Q^* is mostly similar amongst all quadrants, with Q_2 and Q_4 retaining marginally larger values.

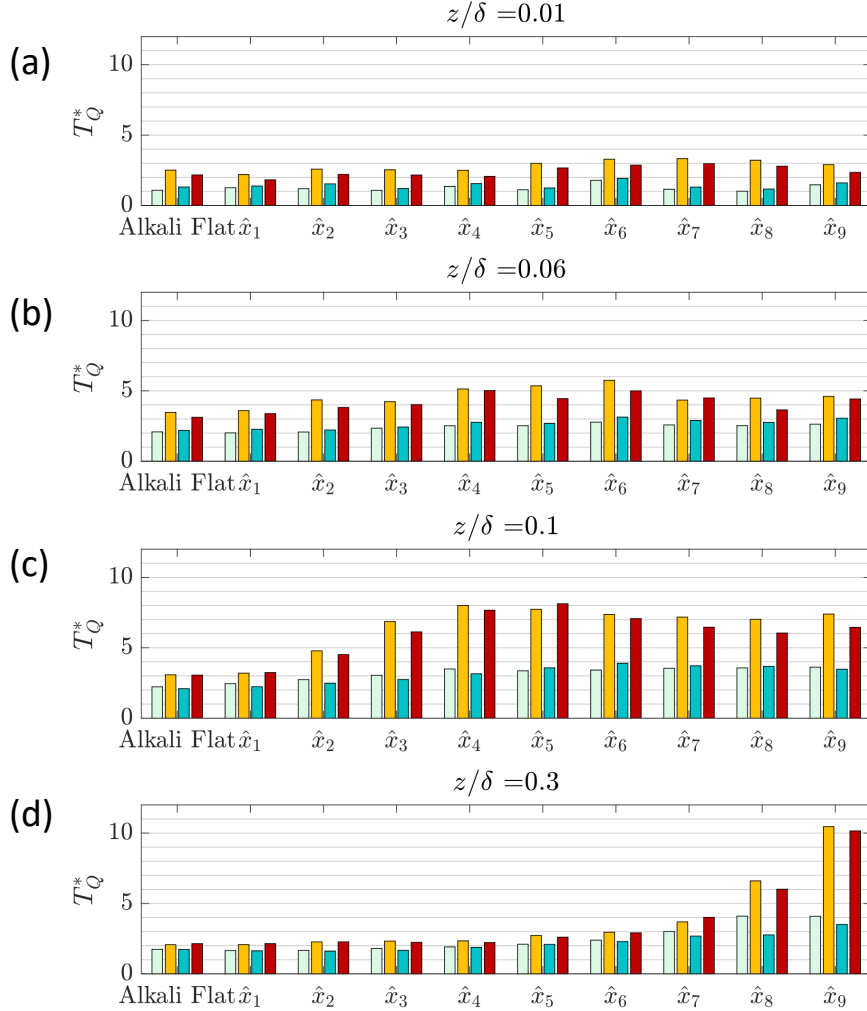


Figure 11. Average dimensionless time duration of quadrant events, T_Q^* , at each probing station, at distinct relative heights z/δ . Bars and colors are the same as in Figure 10 (a) $z/\delta = 0.01$, (b) $z/\delta = 0.06$, (c) $z/\delta = 0.1$, and (d) $z/\delta = 0.3$.

Lastly, we analyze the average event impulse strength, J_Q , in non-dimensional form, J_Q^* (Equation 7). We use the same values for U_∞ and k_a as was used for T_Q^* , and additionally the average friction velocity over the whole dune field, $u_{\tau,02}$. We begin by first looking at the evolution in the Alkali Flat. Beginning with $z/\delta = 0.01$ (Fig. 12a), where, despite the low magnitude, it is clear that Q_2 and Q_4 events have higher average impulse values compared to Q_1 and Q_3 events. Further, at $z/\delta = 0.06$ (Fig. 12b), the magnitude of J_Q^* has significantly increased, especially for Q_2 and Q_4 events, but as was seen

with T_Q^* , at the ASL height (Fig. 12c) and above (Fig. 12d), the average impulse decreases for all events. Much like T_Q^* , J_Q^* follows similar trends observed within the dune field too. For $z/\delta = 0.01$ (Fig. 12a), J_Q^* maintains larger values for Q_2 and Q_4 events, compared to Q_1 and Q_3 events, at all \hat{x} . Moreover, just as was observed with frequency of events and T_Q^* , the largest J_Q^* values for Q_2 and Q_4 events at this elevation occurs between \hat{x}_5 to \hat{x}_8 . Moving to $z/\delta = 0.06$ (Fig. 12b), Q_2 and Q_4 events continue to display larger values of J_Q^* , with Q_2 events consistently having the highest magnitudes. Similar to T_Q^* , the largest values for J_Q^* are found between \hat{x}_4 and \hat{x}_6 . Next, at $z/\delta = 0.1$ (Fig. 12c), values of J_Q^* at \hat{x}_1 mimic those found in the Alkali Flat, and then begin to increase at \hat{x}_2 and \hat{x}_3 . Again, the largest values for J_Q^* at this elevation are also contained within \hat{x}_4 and \hat{x}_6 . Finally, at $z/\delta = 0.3$ (Fig. 12d), the magnitude of J_Q^* is very low, until \hat{x}_7 where the IBL height begins to surpass $z/\delta = 0.3$. Additionally, we observe a large disparity between the magnitudes of average impulse for Q_2 and Q_4 events.

Through visualization of the vortex structures in the dune field, we are better able to connect what we have observed with the evolution of event frequency, T_Q^* , and J_Q^* after the roughness transition. We use the λ_2 -criterion proposed by Jeong and Hussain (1995) for visualizing three dimensional coherent vortical structures, which are colored by instantaneous $u'w'$. We compare two 1-km sections of the dune field: the first ~ 1 kilometer in which the dunes are initially developing, and approximately between the second and third kilometers, in which the dunes are near their largest values of \hat{k}_a . Beginning over the first kilometer (Fig. 13a) of the dune field, the flow initially shows low magnitudes of the Reynolds shear stress, with increasing (in magnitude) value as the flow approaches the larger downstream dunes. Once the flow has reached between the second and third kilometers of the dune field (Fig. 13b), we observe both an increase in the magnitude of the Reynolds shear stress and larger vortex structures away from the wall. Here, this increase of $u'w'$ corresponds with larger observed values of T_Q^* and J_Q^* at $z/\delta = 0.01$ to 0.1.

4.4 Self-Similarity of Q_2 and Q_4 Events in the IBL

We now observe changes to T_Q^* and J_Q^* with plots of their wall-normal distributions throughout the ABL after the roughness transition, specifically for Q_2 and Q_4 events. First, we review T_2^* (Fig. 14a) and T_4^* (Fig. 14b), the average time-duration for events associated with ejections and sweeps, respectively. When plotted against z/δ (insets of Fig. 14a and Fig. 14b), there is a clear thickening of the profiles, with event duration increasing and maintaining elevated values at larger z/δ farther from the roughness transition. Magnitudes for T_2^* and T_4^* are nearly the same at all wall-normal locations, and begin to converge to $T_2^* \approx T_4^* \approx 2$ shortly above $z/\delta = 0.5$ for all \hat{x} . Noticeably, for both T_2^* and T_4^* , profiles at \hat{x}_8 and \hat{x}_9 contain an inner peak and a secondary outer peak farther from the wall. Profiles of T_2^* and T_4^* are next scaled by the local IBL thickness. We observe a reasonable alignment of T_2^* and T_4^* peak values, which indicates that the largest values of T_Q^* occur at a similar scaled elevation, $z/\hat{\delta} \approx 0.5$. Moreover, the values of T_2^* and T_4^* begin to decrease and approach their equilibrium state around $z/\hat{\delta} = 1$.

We plot J_2^* (Fig. 15a) and J_4^* (Fig. 15b) versus z/δ (insets of Fig. 15). With increasing distance from the roughness transition, there is an increase in magnitude at similar z/δ for J_2^* and J_4^* , resulting in a thicker profile further from the wall. Unlike T_Q^* , there are clear differences between the magnitudes of J_2^* and J_4^* . For the Alkali Flat and \hat{x}_1 through \hat{x}_3 , values for J_2^* and J_4^* are similar; however, for \hat{x}_4 and further downstream, magnitudes of J_2^* become much larger than those for J_4^* at similar z/δ . Additionally, the secondary peak observed for T_2^* and T_4^* is only observed for J_2^* . Now, when J_2^* and J_4^* are plotted against $z/\hat{\delta}$, as with T_2^* and T_4^* , there is a reasonable self-similarity of the peak location. Here, the peaks of J_2^* collapse around $z/\hat{\delta} \approx 0.5$ while those of J_4^* do

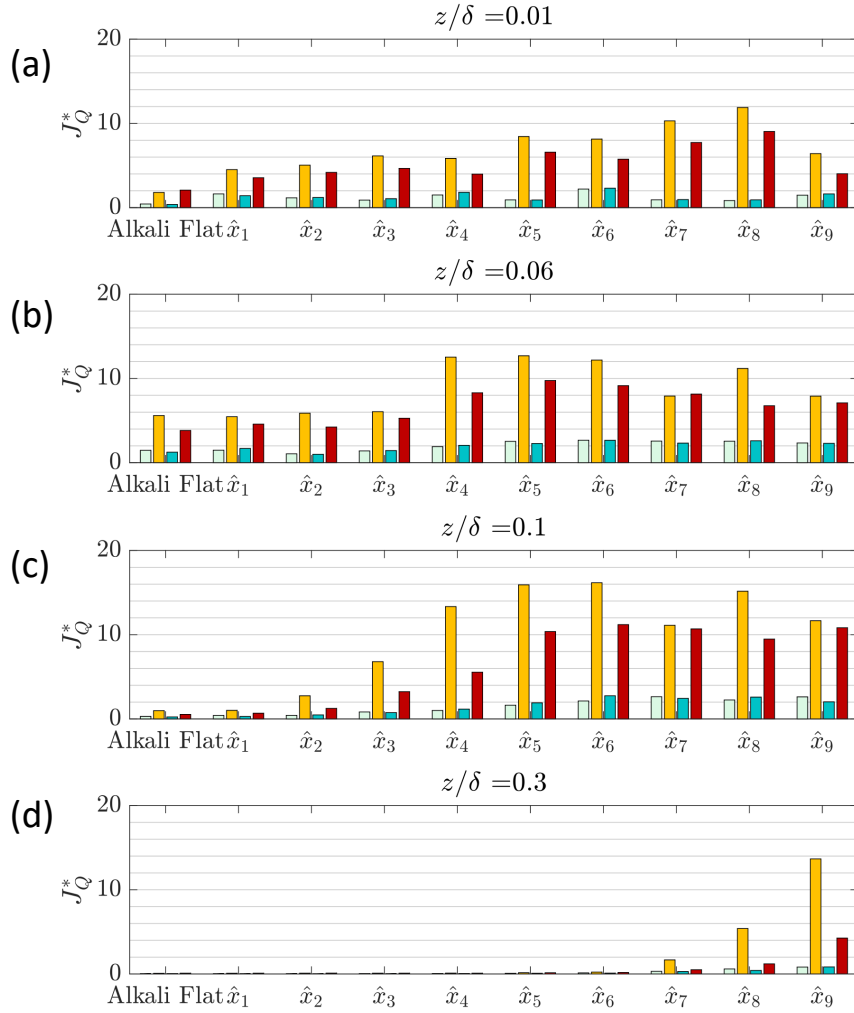


Figure 12. Average impulse strength of quadrant events, J_Q^* , for each probing station, at distinct relative heights z/δ . Bars and colors are the same as in Figure 10. (a) $z/\delta = 0.01$, (b) $z/\delta = 0.06$, (c) $z/\delta = 0.1$, and (d) $z/\delta = 0.3$.

so near $z/\hat{\delta} \approx 0.3$. For both J_2^* and J_4^* , values begin to diminish to zero near $z/\hat{\delta} = 1$.

5 Discussion

Our main result is the demonstration that the IBL height δ_i controls the fundamental scales of turbulence within it, even over a natural and heterogeneous roughness transition. Here we first consider how our results compare to previous findings in less ‘messy’ systems. For the smooth-to-rough transition examined here, we find that beneath δ_i there is region of enhanced Reynolds stresses that thickens as the IBL develops downwind (Fig. 6b). This increase in energy was accompanied by enhancements of sweep (Q_4)

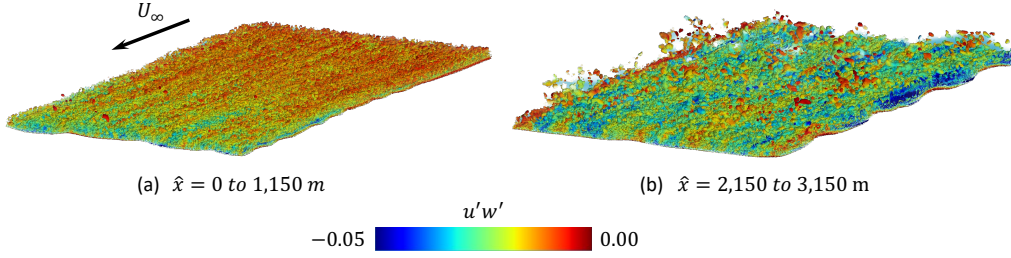


Figure 13. Instantaneous iso-structures of λ_2 -criterion, colored by instantaneous values of $u'w'$. (a) For $\hat{x} = 0 - 1,150$ m (\hat{x}_1 to \hat{x}_3), the dunes are only beginning to develop over the first kilometer, resulting in initially smaller structures and lower magnitudes of $u'w'$. (b) Downstream at $\hat{x} = 2,150 - 3,150$ m (\hat{x}_6 and \hat{x}_7), the dunes are near their largest values of \hat{k}_a . Correspondingly, the flow has adjusted, resulting in large vortex structures and enhanced values of $u'w'$. Flow is from the upper-right to the bottom-left in both (a) and (b).

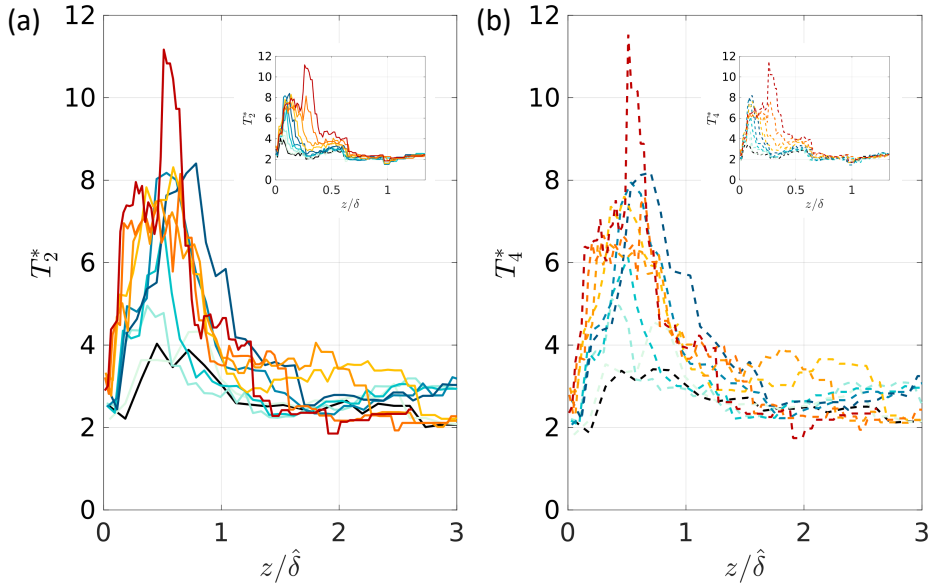


Figure 14. Self-similarity of profiles of T_Q^* for Q_2 (solid lines) and Q_4 (dashed lines) after the roughness transition. (a) Profiles of T_2^* are plotted with wall-normal location normalized by $\hat{\delta}$, as described previously. Using this normalization results in an alignment of the location where the longest average events occur within the IBL. (b) Profiles of T_4^* are plotted in the same manner as (a). Both use the same colors and normalization as Figure 6b. Inset contains the same profiles normalized with a fixed δ , using the same colors and lines styles.

and ejection (Q_2) motions (Figs. 7 and 8), whose magnitude and wall-normal height change systematically with IBL thickness (Figs. 14 and 15). Gul and Ganapathisubramani (2022) reported qualitatively similar observations, for Reynolds stress profiles and sweep and ejection in events, in experiments of IBL development over a step increase in roughness (their Fig. 1f). We observed that both Q_2 and Q_4 events increased in frequency within the IBL,

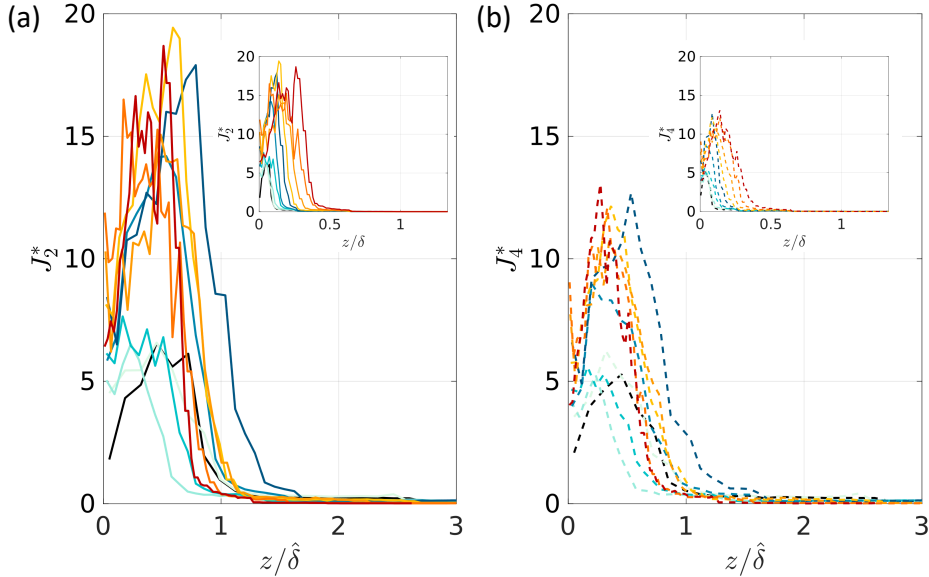


Figure 15. Self-similarity of profiles of J_Q^* for Q_2 (solid lines) and Q_4 (dashed lines) after the roughness transition. (a) Profiles of J_2^* are plotted with wall-normal location normalized by $\hat{\delta}$, as described previously. Using this normalization results in an alignment of the location where the largest average impulse for each event occur within the IBL. (b) Profiles of J_4^* are plotted in the same manner as (a). Both use the same colors, normalization, and line-styles as Figure 14. Inset contains the same profiles normalized with δ , using the same colors and lines styles.

with Q_4 events occurring at a higher frequency than Q_2 events; this pattern was also seen in a wind-tunnel model canopy by Zhu et al. (2007). As these sweeps originate from large-scale, high-speed fluid motions in the outer-layer, this behavior is to be expected (Bristow et al., 2021; Salesky & Anderson, 2018). We found that the duration and impulse of sweep and ejection events were also much larger within the IBL, with the impulse associated with Q_2 events being dominant (Figs. 11 and 12). In their experiments examining flow over an isolated barchan dune, Bristow et al. (2021) found that Q_4 events dominate closer to the dune while Q_2 events are dominant farther from the wall. Although our results contrast with their findings – as we do not observe stronger average impulse strength for Q_4 events nearest wall – our numerical data do not probe directly above the center line of a single dune. More, we do not have access to the flow within the viscous and buffer layers due to the high Re_τ . It is possible also that wall-normal turbulence profiles are different above a train of dunes compared to an isolated dune, because the flow in any location is influenced by the wakes of numerous roughness elements upwind. Examining the difference in flow over an isolated dune, and that same dune embedded in a dune field, would be a useful next step.

The most novel aspect of our study is the quantitative demonstration of how IBL thickness sets the scales of turbulence in the developing flow after a natural smooth-to-rough transition. IBL thickness δ_i sets the eddy turnover time and the energy contained at the largest scales (lowest frequencies in Fig. 9). In other words, the IBL acts as lid that sets the scale of the largest eddies within it, and this scale grows downwind as the IBL thickens. Plotting $\langle u'w' \rangle$ against $z/\hat{\delta}$ (Fig. 6c) shows that the IBL sets the height of the Reynolds shear stress, as the point in which $\langle u'w' \rangle \rightarrow 0$ is $\approx z/\delta_i = 1$. To identify the mechanism behind this, we examined the turbulence producing motions that con-

tribute to $\langle u'w' \rangle$. With quadrant analysis (Fig. 7), we observed the increased magnitude and frequency of u' and w' , resulting in a higher frequency of turbulent producing motions further from the wall. Additionally, we found more frequent Q_2 and Q_4 motions with increasing distance from $\hat{x} = 0$ m (Fig. 10). When using δ to scale the wall-normal elevation, a thickening of the profiles downstream of the roughness transition was observed, indicating the IBL increased the magnitude of T_Q^* and J_Q^* further from the surface (Inset of Figs. 14 and 15). Moreover, when $\hat{\delta}$ was used to scale wall-normal elevation, the point where the ‘peaks’ of T_Q^* and J_Q^* occur collapsed to approximately the same relative point within the IBL (Figs. 14 and 15). The location of these peaks corresponds to the same location within the IBL, $z/\hat{\delta} \approx 0.5$, where we previously observed a peak negative correlation in the amplitude modulation coefficient (Cooke et al., 2024). Previous experimental work has correlated extreme values of sweep and ejection events with increased intermittency (Nakagawa & Nezu, 1977; H. Zhang et al., 2023). This leads to turbulent motions near the wall that are anti-correlated with the motions of the outer flow (Mathis et al., 2009), producing a large negative peak in the amplitude modulation coefficient R_{AM} . The convergence of the mean longest and strongest Q_2 and Q_4 events, with the peak negative correlation of R_{AM} , corroborates these previous findings, and suggests that sweep and ejection events push the intermittency peak away from the wall with increasing \hat{x} .

We note that, although we observed an increase in profiles of T_Q^* and J_Q^* (Figs. 14 and 15), when we isolate z/δ closest to the surface ($z/\delta = 0.06$ and 0.1) and observe changes in \hat{x} (Figs. 11 and 12), the values tended to peak at where \hat{k}_a is also largest. For rough wall-bounded flows, the region of the flow where the effects of roughness are most felt is the roughness sublayer, which extends $2-3k$ above the roughness and into the flow (Chung et al., 2021; Jiménez, 2004). Given the comparatively low height of δ_i as it develops, the larger magnitudes of T_Q^* and J_Q^* observed at these locations respective to those further downstream could be attributed to the larger values of \hat{k}_a . Hence, the IBL acts as an intermediate length-scale, bounded below by the roughness and viscous length-scales, and above by the larger length-scales associated with the outer ABL.

Our simulation results help to explain the observed patterns of dune migration and sediment transport across the White Sands dune field. There is much evidence for turbulence-producing motions contributing to sediment transport in the near-bed region. We point out that our simulations do not include particles or particle transport; the results presented are used to infer how these motions may affect sediment transport. Such attempts for inferences from frozen (or quasi-steady) surfaces are not new, with recent experimental and numerical studies taking this approach (Bristow et al., 2021, 2022; Rana et al., 2021). Field observations by Bauer et al. (1998); Leenders et al. (2005); Schönfeldt and von Löwis (2003), and Sterk et al. (1998) found sweeping motions were most responsible for initiating and sustaining sediment transport. For flows over an individual dune, Wiggs and Weaver (2012) found evidence that sweeping motions were most responsible for entrainment of sand particles and sediment transport. More recently, work from Tan et al. (2023) investigated sediment transport over the rough surface of the Gobi Desert with a quadrant analysis framework, and determined that, similar to rivers with rough gravel beds, sweep events are major contributors to sediment transport. Additionally, experimental wind tunnel work from Xiao-Hu et al. (2024) determined that sufficiently energized sweep events are necessary for entrainment of particles, as weaker sweep events will not prevent the particle from returning to its initial rest position. We find that the IBL enhances these sweep and ejection motions. At the start of the dune field the peaks in sweep and ejection events are close to the wall; however, as the IBL thickens, these peaks gradually move away from the wall. This pattern may explain our previous observation (Cooke et al., 2024) that, after an initial increase at the start of the dune field, the boundary stress gradually declines downwind. A similar pattern was reported for sediment transport by Gunn et al. (2020). As the IBL grows, so does the distance between the surface and the location of the longest and strongest events responsible – and suf-

ficient enough – for sediment transport. Shortly after $\hat{x} = 0$ m, the initial IBL growth and subsequent turbulent motions enhance the sediment transport there, but as the IBL thickens these turbulence producing motions migrate away from the wall, resulting in the gradual decline of sediment transport downwind. These turbulent motions also influence the transport of other particulates, including dust and aerosols. In the saltation process, the impact of individual sand grains on the bed can release dust trapped within (Rana et al., 2021; Shao et al., 2020; Klamt et al., 2024). In their study, Rana et al. (2021) showed that regions of high momentum – generally characterized by sweeping motions – enable both saltation and, indirectly, dust entrainment. Additionally, Shao et al. (2020) confirmed the dependence of dust particle size distribution on u_τ , and indicated that stronger turbulence, which results in larger mean values of u_τ and greater variance, would result in increased saltation-bombardment and dust emission. As our results indicate, the increased frequency of sweeping motions has the potential to increase dust emission, especially nearest the roughness transition. Moreover, as the strongest motions move further from the wall, so too could the potential for the entrained dust to be carried away from the surface by these motions. Although all the findings here pertain to simulations of turbulent flow over a natural dune field, the discovery that IBL thickness scales the profile of turbulent producing motions is a result that we expect may generalize to other ABL flows over roughness transitions. For urban topography where low-lying buildings transition to high-rise skyscrapers, this rough-to-rougher transition will see an enhancement to turbulence producing motions and changes to thermal stratification, with the capacity to augment the transport of momentum, particles, heat, and moisture (Sessa et al., 2020; Rios & Ramamurthy, 2023). The developing IBL at the land-ocean interface exerts a control on moisture transport (Jiang & Wang, 2021). Finally, roughness transitions such as field to forest canopy should also produce similar behaviors, influencing the transport of moisture and CO₂, as turbulent mixing over forest canopies is enhanced (Baldocchi, 2003). The deployment of eddy flux towers should explicitly account for IBL development, which produces spatially varying turbulence motions over distances of many kilometers.

6 Conclusion

We performed Wall-Modeled Large-Eddy Simulation (WMLES) of a neutrally buoyant Atmospheric Boundary Layer (ABL) encountering a roughness transition between a smooth playa and a spatially heterogeneous dune field. Our simulations captured the development of an Internal Boundary Layer (IBL) which forms at the inception of the dune field. Using observations of the energy frequency spectrum of the streamwise velocity fluctuations $E(\omega)$ at multiple locations downstream of the roughness transition, we show how the IBL sets the low frequencies (large scales) of turbulence. Additionally, we calculate a frequency associated with the IBL, and find it correlates well with the scaling break in the energy frequency spectrum, typically associated with the largest-scale eddy turnover time. As a result of the IBL setting the largest scales, we show how the IBL enhances turbulence producing motions throughout, especially ejection (Q_2) and sweep (Q_4) events. Moreover, these events display a self-similarity at subsequent downstream locations, in both the average event time-duration (T_Q^*) and impulse strength (J_Q^*). As the location of the longest and strongest of these events migrates away from the wall with the growing IBL, the enhancement of sediment flux, and transport of other materials, over the initial portion of the dune field is lost downstream. For ABL flows encountering roughness transitions, δ_i is clearly a prominent mesoscopic length scale; its spatial growth scales the profile of many turbulent characteristics that are not captured with inner- or outer-scalings. It would be beneficial to deploy this scaling for other roughness transitions – rough-to-smooth, rough-to-rougher, and vice versa – to see if it is universal. Additionally, our WMLES does not capture the near-surface flow characteristics, as the high Re_τ incurs a high computational cost. A direct numerical simulation, or ex-

perimental study, at a more moderate Re_τ would allow for examining the efficacy of this scaling closer to the wall.

Acknowledgments

G.P. and J.C. acknowledge the support from the University of Pennsylvania (faculty startup grant and the Fontaine Fellowship) and the National GEM Consortium Fellowship. D.J.J. was supported by NASA PSTAR (Award 80NSSC22K1313). We would also like to acknowledge Prof. Andrew Gunn for helpful discussions related to his work at White Sands, and for providing his experimental data. The authors declare no conflict of interest related to this work, financial or otherwise.

References

- Abedi, H., Sarkar, S., & Johansson, H. (2021). Numerical modelling of neutral atmospheric boundary layer flow through heterogeneous forest canopies in complex terrain (a case study of a Swedish wind farm). *Renewable Energy*, *180*, 806–828.
- Ambo, K., Nagaoka, H., Philips, D. A., Ivey, C. B., Brès, G. A., & Bose, S. T. (2020). Aerodynamic force prediction of the laminar to turbulent flow transition around the front bumper of the vehicle using dynamic-slip wall model LES. In *AIAA SciTech Forum*.
- Anderson, W., & Chamecki, M. (2014). Numerical study of turbulent flow over complex aeolian dune fields: The White Sands National Monument. *Physical Review E*, *89*, 013005.
- Antonia, R., & Luxton, R. (1972a). The response of a turbulent boundary layer to a step change in surface roughness part 1. smooth to rough. *Journal of Fluid Mechanics*, *48*, 721–761.
- Antonia, R., & Luxton, R. (1972b). The response of a turbulent boundary layer to a step change in surface roughness. part 2. rough to smooth. *Journal of Fluid Mechanics*, *53*, 737–757.
- Bagnold, R. A. (1941). *The physics of blown sand and desert dunes*. Methuen & Co.
- Baldocchi, D. D. (2003). Assessing the eddy covariance technique for evaluating carbon dioxide exchange rates of ecosystems: past, present and future. *Global change biology*, *9*(4), 479–492.
- Bauer, B. O., Walker, I. J., Baas, A. C., Jackson, D. W., Neuman, C. M., Wiggs, G. F., & Hesp, P. A. (2013). Coherent flow structures at earth’s surface. In (pp. 111–134). John Wiley & Sons.
- Bauer, B. O., Yi, J., Namikas, S. L., & Sherman, D. J. (1998). Event detection and conditional averaging in unsteady aeolian systems. *Journal of Arid Environments*, *39*(3), 345–375.
- Bell, T. M., Greene, B. R., Klein, P. M., Carney, M., & Chilson, P. B. (2020). Confronting the boundary layer data gap: evaluating new and existing methodologies of probing the lower atmosphere. *Atmospheric Measurement Techniques*, *13*, 3855–3872.
- Bodart, J., & Larsson, J. (2011). Wall-modeled large eddy simulation in complex geometries with application to high-lift devices. In *Center for turbulence research annual research briefs*.
- Bodony, D. (2006). Analysis of sponge zones for computational fluid mechanics. *Journal of Computational Physics*, *212*, 681–02.
- Bou-Zeid, E., Anderson, W., Katul, G. G., & Mahrt, L. (2020). The persistent challenge of surface heterogeneity in boundary-layer meteorology: a review. *Boundary-Layer Meteorology*, *177*, 227–245.
- Brès, G. A., Ivey, C. B., Philips, D. A., Bose, S. T., Miyazawa, M., Morishita, K.,

- & Teramura, M. (2023). Aeroacoustic simulations of full-scale sedan vehicle towards interior noise predictions. In *AIAA Aviation 2023 Forum*.
- Bristow, N. R., Best, J., Wiggs, G. F. S., Nield, J. M., Baddock, M. C., Delorme, P., & Christensen, K. T. (2022). Topographic perturbation of turbulent boundary layers by low-angle, early-stage aeolian dunes. *Earth Surface Processes and Landforms*, *47*, 1439–1454.
- Bristow, N. R., Blois, G., Best, J. L., & Christensen, K. T. (2021). Unsteady dynamics of turbulent flow in the wakes of barchan dunes modulated by overlying boundary-layer structure. *Journal of Fluid Mechanics*, *920*, A51-1–A51-39.
- Ceamanos, X., Coopman, Q., George, M., Riedi, J., parrington, M., & Clerbaux, C. (2023). Remote sensing and model analysis of biomass burning smoke transported across the Atlantic during the 2020 Western US wildfire season. *Scientific Reports*, *13*.
- Choi, H., Moin, P., & Kim, J. (1993). Direct numerical simulation of turbulent flow over riblets. *Journal of Fluid Mechanics*, *255*, 503–539.
- Chung, D., Hutchins, N., Schultz, M., & Flack, K. (2021). Predicting the drag of rough surfaces. *Annual Reviews*, *53*, 439–471.
- Cooke, J. P., Campbell, M. F., Steager, E. B., Bargatin, I., Yim, M. H., & Park, G. I. (2023). Numerical and experimental study on the addition of surface roughness to micro-propellers. *Physics of Fluids*, *35*, 113607.
- Cooke, J. P., Jerolmack, D. J., & Park, G. I. (2024). Mesoscale structure of the atmospheric boundary layer across a natural roughness transition. *Proceedings of the National Academy of Sciences*, *121*(13), 2320216121.
- Elliott, W. P. (1958). The growth of the atmospheric internal boundary layer. *Eos, Transactions American Geophysical Union*, *39*, 1048–1054.
- Fernholz, H., & Finley, P. (1996). The incompressible zero-pressure-gradient turbulent boundary layer: an assessment of the data. *Progress in Aerospace Sciences*, *32*(4), 245–311.
- Gadal, C., Narteau, C., Ewing, R., Gunn, A., Jerolmack, D., Andreotti, B., & Claudin, P. (2021). Spatial and temporal evolution of incipient dunes. *Geophysical Research Letters*, *47*, e2020GL088919.
- Gould, C. F., Heft-Neal, S., Prunicki, M., Aguilera, J., Burke, M., & Nadeau, K. (2024). Health effects of wildfire smoke exposure. *Annual Review of Medicine*, *75*.
- Gul, M., & Ganapathisubramani, B. (2022). Experimental observations on turbulent boundary layers subjected to a step change in surface roughness. *Journal of Fluid Mechanics*, *947*, A6-1–A6-25.
- Gunn, A., Casasanta, G., Di Liberto, L., Falcini, F., Lancaster, N., & Jerolmack, D. J. (2022). What sets aeolian dune height? *Nature Communications*, *13*, 2401.
- Gunn, A., Schmutz, P., Wanker, M., Edmonds, D., Ewing, R., & Jerolmack, D. (2020). Macroscopic flow disequilibrium over aeolian dune fields. *Geophysical Research Letters*, *47*.
- Gunn, A., Wanker, M., Lancaster, N., Edmonds, D., Ewing, R., & Jerolmack, D. (2021). Circadian rhythm of dune-field activity. *Geophysical Research Letters*, *48*.
- Hanson, R., & Ganapathisubramani, B. (2016). Development of turbulent boundary layers past a step change in wall roughness. *Journal of Fluid Mechanics*, *795*, 494–523.
- Hayat, I., & Park, G. (2023). Wall-modeled large-eddy simulation of turbulent boundary layer with spatially varying pressure gradients. *AIAA Journal*.
- Hu, X., Hayat, I., & Park, G. (2023). Wall-modelled large-eddy simulation of three-dimensional turbulent boundary layer in a bent square duct. *Journal of Fluid Mechanics*, *960*.
- Hwang, J., Lee, J., Sung, H., & Zaki, T. (2016). Inner-outer interactions of large-

- scale structures in turbulent channel flow. *Journal of Fluid Mechanics*, 790, 128–157.
- Hwang, Y., & Gorlé, C. (2022). Large-eddy simulations of wind-drive cross ventilation, part 1: validation and sensitivity study. *Frontiers in Built Environment*, 8, 911005.
- Hwang, Y., & Gorlé, C. (2023). Large-eddy simulations to define building-specific similarity relationships for natural ventilation flow rates. *Flow*, 3, E10.
- Jeong, J., & Hussain, F. (1995). On the identification of a vortex. *Journal of Fluid Mechanics*, 285, 63–94.
- Jerolmack, D., Ewing, R., Falcini, F., Martin, R., Masteller, C., Phillips, C., . . . Buynevich, I. (2012). Internal boundary layer model for the evolution of desert dune fields. *Nature Geoscience*, 5(3), 206–209.
- Jiang, Q., & Wang, Q. (2021). Characteristics and scaling of the stable marine internal boundary layer. *Journal of Geophysical Research: Atmospheres*, 126(21), e2021JD035510.
- Jiménez, J. (2004). Turbulent flows over rough walls. *Annual Review of Fluid Mechanics*, 36, 173–196.
- Kawai, S., & Larsson, J. (2012). Wall-modeling in large eddy simulation: Length scales, grid resolution, and accuracy. *Physics of Fluids*, 24, 015105.
- Klamt, J., Giersch, S., & Raasch, S. (2024). Saltation-induced dust emission of dust devils in the convective boundary layer—an les study on the meter scale. *Journal of Geophysical Research: Atmospheres*, 129(7), e2023JD040058.
- Klein, M., Sadiki, A., & Janicka, J. (2003). A digital filter based generation of inflow data for spatially developing direct numerical or large eddy simulations. *Journal of Computational Physics*, 186(2), 652–655.
- Kok, J. F., Parteli, E. J., Michaels, T. I., & Karam, D. B. (2012). The physics of wind-blown sand and dust. *Reports on progress in Physics*, 75(10), 106901.
- Lee, D., Ferdowsi, B., & Jerolmack, D. (2019). The imprint of vegetation on desert dune dynamics. *Geophysical Research Letters*, 46(21), 12041–12048.
- Leenders, J. K., van Boxel, J. H., & Sterk, G. (2005). Wind forces and related saltation transport. *Geomorphology*, 71, 357–372.
- Li, D., & Bou-Zeid, E. (2013). Synergistic interactions between urban heat islands and heat waves: the impact in cities is larger than the sum of its parts*. *Journal of Applied Meteorology and Climatology*, 52(9), 2051–2064.
- Li, M., de Silva, C. M., Chung, D., Pullin, D. I., Marusic, I., & Hutchins, N. (2021). Experimental study of a turbulent boundary layer with a rough-to-smooth change in surface conditions at high Reynolds numbers. *Journal of Fluid Mechanics*, 923, A18-1–A18-41.
- Li, Q., & Bou-Zeid, E. (2019). Contrasts between momentum and scalar transport over very rough surfaces. *Journal of Fluid Mechanics*, 880, 32–58.
- Li, W., & Giometto, M. (2023). Mean flow and turbulence in unsteady canopy layers. *Journal of Fluid Mechanics*, 974, A33.
- Lin, C.-L., Moeng, C.-H., & Sullivan, P. (1997). The effect of surface roughness on flow structures in a neutrally stratified planetary boundary layer flow. *Physics of Fluids*, 9, 3235–3249.
- Mani, A. (2012). Analysis and optimization of numerical sponge layers as a non-reflective boundary treatment. *Journal of Computational Physics*, 231, 704–715.
- Manoli, G., Fatichi, S., Schläpfer, M., Yu, K., Crowther, T., Meili, N., . . . Bou-Zeid, E. (2019). Magnitude of urban heat islands largely explained by climate and population. *Nature*, 573, 55–60.
- Mathis, R., Hutchins, N., & Marusic, I. (2009). Large-scale amplitude modulation of the small-scale structures in turbulent boundary layers. *Journal of Fluid Mechanics*, 628, 311–337.
- Nakagawa, H., & Nezu, I. (1977). Prediction of the contributions to the Reynolds stress from bursting events in open-channel flows. *Journal of Fluid Mechanics*,

80, 99–128.

- Panofsky, H. (1973). Tower micrometeorology. In *Workshop on micrometeorology*. American Meteorological Society.
- Panofsky, H., & Dutton, J. (1984). *Atmospheric turbulence*. Wiley (Interscience).
- Parajuli, S. P., Zobeck, T. M., Kocurek, G., Yang, Z.-L., & Stenchikov, G. L. (2016). New insights into the wind-dust relationship in sandblasting and direct aerodynamic entrainment from wind tunnel experiments. *Journal of Geophysical Research: Atmospheres*, *121*(4), 1776–1792.
- Park, G., & Moin, P. (2016). Space-time characteristics of wall-pressure and wall shear-stress fluctuations in wall-modeled large eddy simulation. *Physical Review Fluids*, *1*, 024404.
- Pendergrass, W., & Aria, S. (1984). Dispersion in neutral boundary layer over a step change in surface roughness - i. mean flow and turbulence structure. *Boundary Layer Meteorology*, *18*, 1267–1279.
- Rana, S., Anderson, W., & Day, M. (2021). "an entrainment paradox: how hysteretic saltation and secondary transport augment atmospheric uptake of aeolian source materials". *Journal of Geophysical Research: Atmospheres*, *126*, e2020JD033493.
- Raupach, M. R. (1981). Conditional statistics of reynolds stress in rough-wall and smooth-wall turbulent boundary layers. *Journal of Fluid Mechanics*, *108*, 363–382.
- Reitz, M., Jerolmack, D., Ewing, R., & Martin, R. (2010). Barchan-parabolic dune pattern transition from vegetation stability threshold. *Geophysical Research Letters*, *37*(19), L19402.
- Rios, G., & Ramamurthy, P. (2023). Turbulence in the mixed layer over an urban area: a new york city case study. *Boundary-Layer Meteorology*, *188*(3), 419–440.
- Salesky, S., & Anderson, W. (2018). Buoyancy effects on large-scale motions in convective atmospheric boundary layers: implications for modulation of near-wall processes. *Journal of Fluid Mechanics*, *856*, 135–168.
- Savel'yev, S., & Taylor, P. (2001). Notes on internal boundary-layer height formula. *Boundary Layer Meteorology*, *101*, 293–301.
- Schönfeldt, H.-J., & von Löwis, S. (2003). Turbulence-driven saltation in the atmospheric surface layer. *Meteorologische Zeitschrift (Berlin)*, *12*.
- Sessa, V., Xie, Z.-T., & Herring, S. (2020). Thermal stratification effects on turbulence and dispersion in internal and external boundary layers. *Boundary-Layer Meteorology*, *176*(1), 61–83.
- Shao, Y., Zhang, J., Ishizuka, M., Mikami, M., Leys, J., & Huang, N. (2020). Dependency of particle size distribution at dust emission on friction velocity and atmospheric boundary-layer stability. *Atmospheric Chemistry and Physics*, *20*(21), 12939–12953.
- Sterk, G., Jacobos, A. F. G., & van Boxel, J. H. (1998). The effect of turbulent flow structures on saltation sand transport in the atmospheric boundary layer. *Earth Surface Processes and Landforms*, *23*, 877–887.
- Stoll, R., Gibbs, J. A., Salesky, S. T., Anderson, W., & Calaf, M. (2020). Large-eddy simulation of the atmospheric boundary layer. *Boundary-Layer Meteorology*, *177*, 541–581.
- Tan, L., Qu, J., Wang, H., An, Z., Wang, T., & Zhao, S. (2023). Turbulent flow structures over a Gobi surface and their impact on aeolian sand transport. *Geophysical Research Letters*, *50*, e2023GL103360.
- Townsend, A. (1965). The response of a turbulent boundary layer to abrupt changes in surface conditions. *Journal of Fluid Mechanics*, *22*(4), 799–822.
- US Geological Survey. (2020). *3d elevation program lidar point cloud*. Online. (Accessed: 9/30/2022 https://portal.opentopography.org/usgsDataset?dsid=NM_SouthEast_B4_2018)

- Vanderwel, C., & Ganapathisubramani, B. (2019). Turbulent boundary layers over multiscale rough patches. *Boundary-Layer Meteorology*, *172*, 1–16.
- Vreman, A. (2004). An eddy-viscosity subgrid-scale model for turbulent shear flow: Algebraic theory and applications. *Physics of Fluids*, *16*, 3670–3681.
- Wallace, J. M. (2016). Quadrant analysis in turbulence research: history and evolution. *Annual Review of Fluid Mechanics*, *48*, 131–158.
- Wallace, J. M., Eckelmann, H., & Brodkey, R. S. (1972). The wall region in turbulent shear flow. *Journal of Fluid Mechanics*, *54*, 39–48.
- Wang, C., & Anderson, W. (2019). Turbulence coherence within canonical and realistic aeolian dune-field roughness sublayers. *Boundary-Layer Meteorology*, *173*, 409–435.
- Wiggs, G. F. S., & Weaver, C. M. (2012). Turbulent flow structures and aeolian sediment transport over a barchan sand dune. *Geophysical Research Letters*, *39*, L05404.
- Willmarth, W. W., & Lu, S. S. (1972). Structure of the reynolds stress near the wall. *Journal of Fluid Mechanics*, *55*, 65–92.
- Wood, D. (1982). Internal boundary layer growth following a step change in surface roughness. *Boundary Layer Meteorology*, *22*, 241–234.
- Xiao-Hu, Z., Valyrakis, M., Pähtz, T., & Zhen-Shan, L. (2024). The role of coherent airflow structures on the incipient aeolian entrainment of coarse particles. *Journal of Geophysical Research: Earth Surface*, *129*(5), e2023JF007420.
- Zhang, H., Tan, X., & Zheng, X. (2023). Multifield intermittency of dust storm turbulence in the atmospheric surface layer. *Journal of Fluid Mechanics*, *963*, A15.
- Zhang, J., Li, G., Shi, L., Huang, N., & Shao, Y. (2022). Impact of turbulence on aeolian sand and dust entrainment: Results from wind-tunnel experiment. *Atmospheric Chemistry & Physics Discussions*.
- Zhou, S., Xu, R., Chen, G., Yu, P., & Guo, Y. (2023). Where is the boundary of wildfire smoke? *The Innovation Medicine*, *1*, 100024.
- Zhu, W., van Hout, R., & Katz, J. (2007). On the flow structure and turbulence during sweep and ejection events in a wind-tunnel model canopy. *Boundary-Layer Meteorology*, *124*, 205–233.